Precipitation in Stratocumulus Clouds: Observational and Modeling Results

PHILIP AUSTIN,* YINONG WANG,* ROBERT PINCUS,** AND VINCENT KUJALA*

*Atmospheric Sciences Programme, University of British Columbia, Vancouver, BC, Canada
**Geophysics Program, University of Washington, Seattle, Washington

(Manuscript received 1 July 1993, in final form 12 July 1994)

ABSTRACT

The spatial and temporal variability of precipitating stratocumulus layers is examined using aircraft observations, satellite retrievals of cloud optical depth, and one-dimensional models that include coalescence and a simple representation of layer turbulence. The aircraft observations show large horizontal variations in cloud thickness and precipitation, with local rain rates 4–5 times larger than the replacement moisture flux, and evidence for precipitation scavenging of small cloud droplets. The satellite observations show that, despite this local water loss, the distribution of cloud optical thickness remains nearly constant over the course of a day, indicating that on larger scales precipitation removal and cloud-top entrainment are in approximate balance with the vapor flux. The authors apply analytic and numerical models of steady-state precipitation to the observed microphysical conditions, and find that the models can match the drop size distributions observed during both heavy and light stratocumulus rainfall, but are especially sensitive to the processes governing the growth rate of the smallest drizzle drops.

1. Introduction

Precipitation in stratocumulus clouds is a principal sink for condensation nuclei and liquid water, and plays an important part in energy transport within the boundary layer. There is current interest in the role of precipitation in thinning the cloud layer and decreasing cloud fraction (Albrecht 1989), in setting the equilibrium boundary layer concentration of cloud condensation nuclei (Baker and Charlson 1989), and in aiding the decoupling of the well-mixed layer through evaporative cooling below cloud (Brost et al. 1982a; Nicholls and Leighton 1986; Paluch and Lenschow 1991).

Previous aircraft observations of stratocumulus precipitation have shown an approximate balance between a 1 mm/day rain rate and the vapor flux through cloud base (Nicholls and Leighton 1986; Brost et al. 1982b), with a roughly linear variation between cloud thickness and the drizzle flux (Nicholls and Leighton 1986). In contrast, a one-dimensional equilibrium model of coalescing, sedimenting raindrops exhibits quite different behavior, suggesting that the rain rate might increase as the fifth power of cloud thickness (Nicholls 1987). Recently, Baker (1993) has developed an analytic version of Nicholls's model that predicts the equilibrium raindrop size distribution given the height within the cloud, the autocorrelation of the vertical velocity, and the rate at which the smallest cloud droplets produce embryonic raindrops (the autoconversion rate).

In this paper we use aircraft and satellite data to measure the water budget and the microphysical character of three precipitating cloud layers. The observations come from the First ISSCP (International Satellite Cloud Climatology Program) Regional Experiment (FIRE) (Albrecht et al. 1988; Kloesel et al. 1988) and include cloud physics measurements from the National Center for Atmospheric Research (NCAR) Electra and the British Meteorological Office C130 aircraft and half-hourly geostationary satellite retrievals of cloud optical depth. We map the spatial and temporal variability of precipitation and cloud thickness for these three cases and link the observed rain rates to the microphysical and turbulent character of the layers. These observations are compared to the predictions of Baker's analytic model and to a one-dimensional numerical model based on Nicholls's equilibrium calculation.

Our objectives are to

- characterize the vertical and horizontal microphysical structure of the three precipitating clouds
- estimate the ability of the stratocumulus layers to initiate coalescence through autoconversion, given representative small droplet distributions
- examine the sensitivity of both the numeric and analytic models to variations in cloud thickness and the small droplet number distribution typical of these clouds

In section 2 we present cloud profiles and precipitation measurements for vertical and horizontal Electra

Corresponding author address: Philip Austin, Atmospheric Sciences Programme, Geography #217, 1984 West Mall, Vancouver, BC V6T 1Z2, Canada.
E-mail: phil@geog.ubc.ca

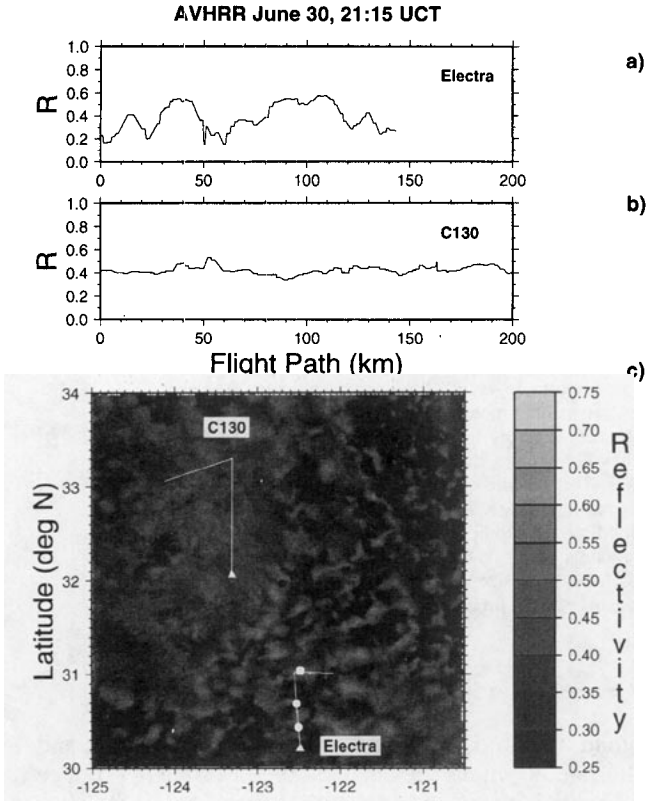

FIG. 1. Marine stratocumulus clouds off the coast of Southern California during FIRE. The image shows the visible reflectance at 22:18 UCT (15:18 PDT) on 30 June 1987, as measured by the Advanced Very High Resolution Radiometer (AVHRR) aboard *NOAA-9*. The straight line indicates the approximate position of Electra flight leg L7, which began ≈25 minutes after the satellite overpass (see Table 1), as well as a C130 flight track near this time. Triangles denote the start of the flight leg, filled circles indicate the location of precipitation maxima observed by the aircraft. (a) Reflectivity along the Electra flight leg, (b) reflectivity along the C130 flight leg, (c) full image.

and C130 penetrations, and the Electra-derived layer water budgets. In section 3 we discuss half-hourly measurements of cloud optical depth in a Lagrangian reference frame advecting with the 1000-hPa flow, while section 4 contains a discussion of the analytic and numeric one-dimensional cloud models applied to FIRE conditions. In section 5 we examine the sensitivity of the modeled precipitation flux to changes in cloud thickness and the coalescence kernel, and section 6 contains a discussion of these results.

2. Aircraft observations

a. Flight plans and conditions

Data from FIRE include in-situ measurements from three aircraft in marine stratocumulus clouds off the coast of California. We will examine NCAR Electra aircraft data for three (of 13) FIRE days. On these days precipitation was a significant component of the boundary layer water budget: 30 June 1987 (Electra flight 2), 14 July 1987 (Electra flight 8), and 16 July 1987 (Electra flight 9). We will also show cloud microphysical observations from C130 soundings located near the Electra flight legs.

Figures 1, 2, and 3 show satellite visible-channel reflectance measurements for the three cases, overlayed with the Electra in-cloud flight legs closest in time to the satellite image. The filled triangles mark the starting point of each flight track. The layers are almost completely cloudy throughout the observing period; for these images the fraction of pixels with directional reflectivities greater than 0.2 in a 256 × 256 km box surrounding the flight leg is 94%, 99%, and 99% for 30 June, 14 July, and 16 July, respectively.

On each of the days the Electra flew in-cloud and below-cloud L-shaped patterns (or an extended in-cloud butterfly and brief linear transects on 14 and 16 July, respectively) of 50–150 km between fixed positions. The L-patterns were oriented along and across the wind, with soundings at the leg ends. Table 1 lists the times, heights, and abbreviations for the flight legs used in this paper. Figure 4 shows the locations for each

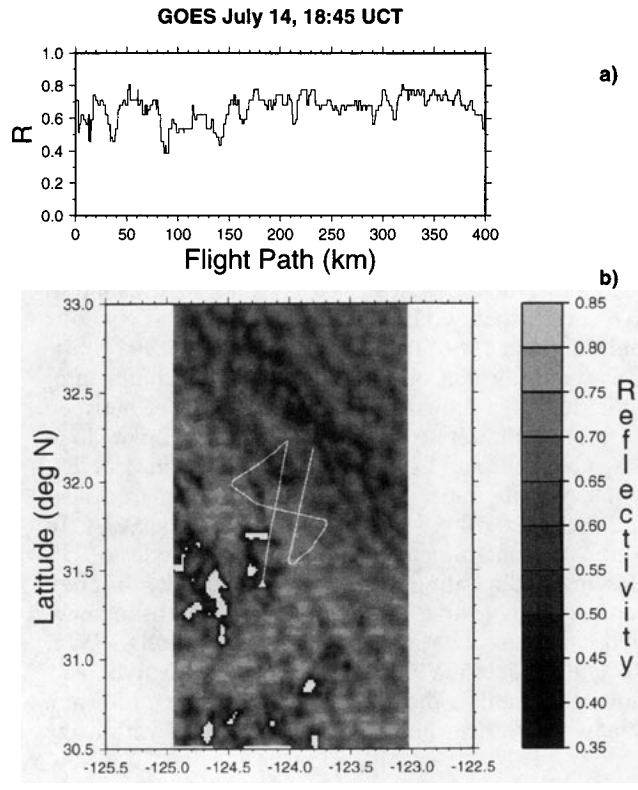

FIG. 2. Visible reflectance measured by the *Geostationary Operational Environmental Satellite* (GOES) -6 Visible Infrared Spin Scan Radiometer (VISSR) at 18:45 UCT (11:45 PDT) on 14 July 1987, and Electra flight leg L0. The image was taken when the flight leg was about half complete. (a) Satellite reflectivities along the flight leg, (b) full image.

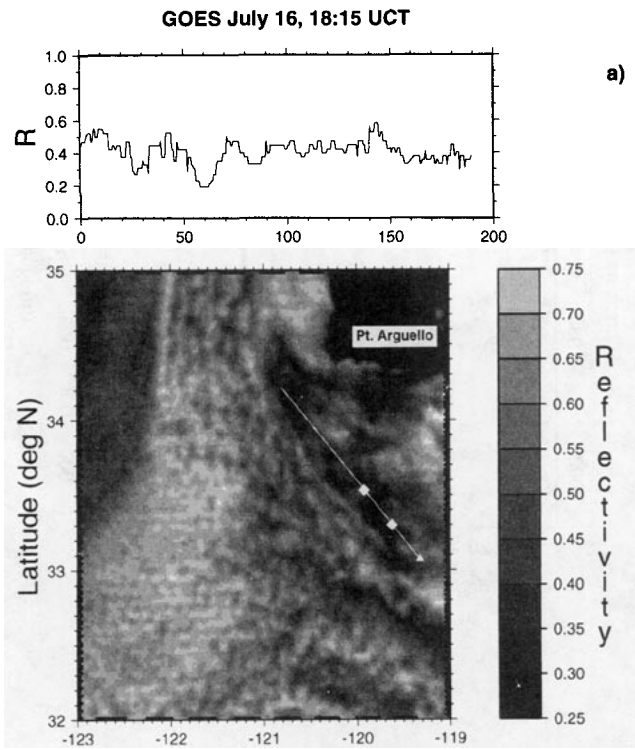

FIG. 3. As in Fig. 2. The image was taken at 18:15 UCT (11:15 PDT) on 16 July 1987. Point Arguello, near Santa Barbara, is visible in the upper right-hand corner. The filled squares show the actual start and finish of the flight leg. (a) Satellite reflectivities along Electra flight leg L2, which began at 18:19 UCT, (b) full image.

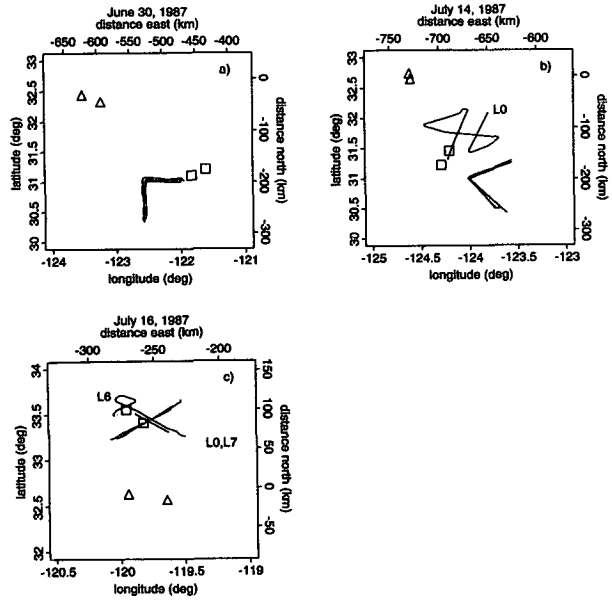

FIG. 4. Location of Electra level legs (lines) plus the start and stop points for the 3 Electra (△) and 3 C130 (□) soundings listed in Table 1.

of the legs in Table 1, as well as the starting and stopping points for six soundings to be discussed in section 2b.

Although navigational uncertainties prohibit a pixel-by-pixel comparison between the in situ and satellite measurements, the projections of the satellite reflectivities along the flight paths (panels b and c in the Figs. 1–3) show significant variations on 20–50-km scales in the vicinity of the Electra. These reflectivity variations have roughly the same spatial scale as the precipitation variations within the layers; the filled circles on Electra leg L7 in Fig. 1 give the locations of a series of in-cloud precipitation maxima for that leg. The different cloud character in the 30 June regions flown by the Electra and C130 is also apparent in Fig. 7; observer reports show no precipitation for the C130 30 June flight legs with droplet concentrations roughly three times greater than those observed by the Electra.

On 14 July the image and the flight track show higher brightness values than for the other days, with reflectivities > 0.6 for most pixels. Additional mesoscale variations in cloud brightness are visible on 16 July, with a transition to thinner cloud west of 122°W lon-

TABLE 1. Altitude z (m) and times (UCT) for Electra flight legs (L0–L7) and Electra and C130 soundings (ES and CS).

30 June				14 July				16 July			
Leg	z (m)	Start	Stop	Leg	z (m)	Start	Stop	Leg	z (m)	Start	Stop
ES	S	19:10	19:14	ES	S	18:11	18:15	CS	S	16:25	16:32
L0	50	19:18	19:38	L0	699	18:18	19:13	ES	S	16:45	16:54
L1	314	19:40	19:59	CS	S	19:43	19:47	L0	50	16:55	17:01
CS	S	19:44	19:49	L1	50	19:50	20:11	L1	625	17:17	17:24
L2	788	20:01	20:20	L2	173	20:12	20:29	L2	631	18:19	18:29
L3	843	20:21	20:32	L3	324	20:29	20:49	L3	492	18:31	18:40
L4	50	21:31	21:51	L4	487	20:51	21:08	L4	92	18:44	18:53
L5	315	21:52	22:12	L5	729	21:08	21:26	L5	101	18:55	19:00
L6	624	22:13	22:34					L6	206	19:22	19:30
L7	789	22:43	23:06					L7	104	19:30	19:40

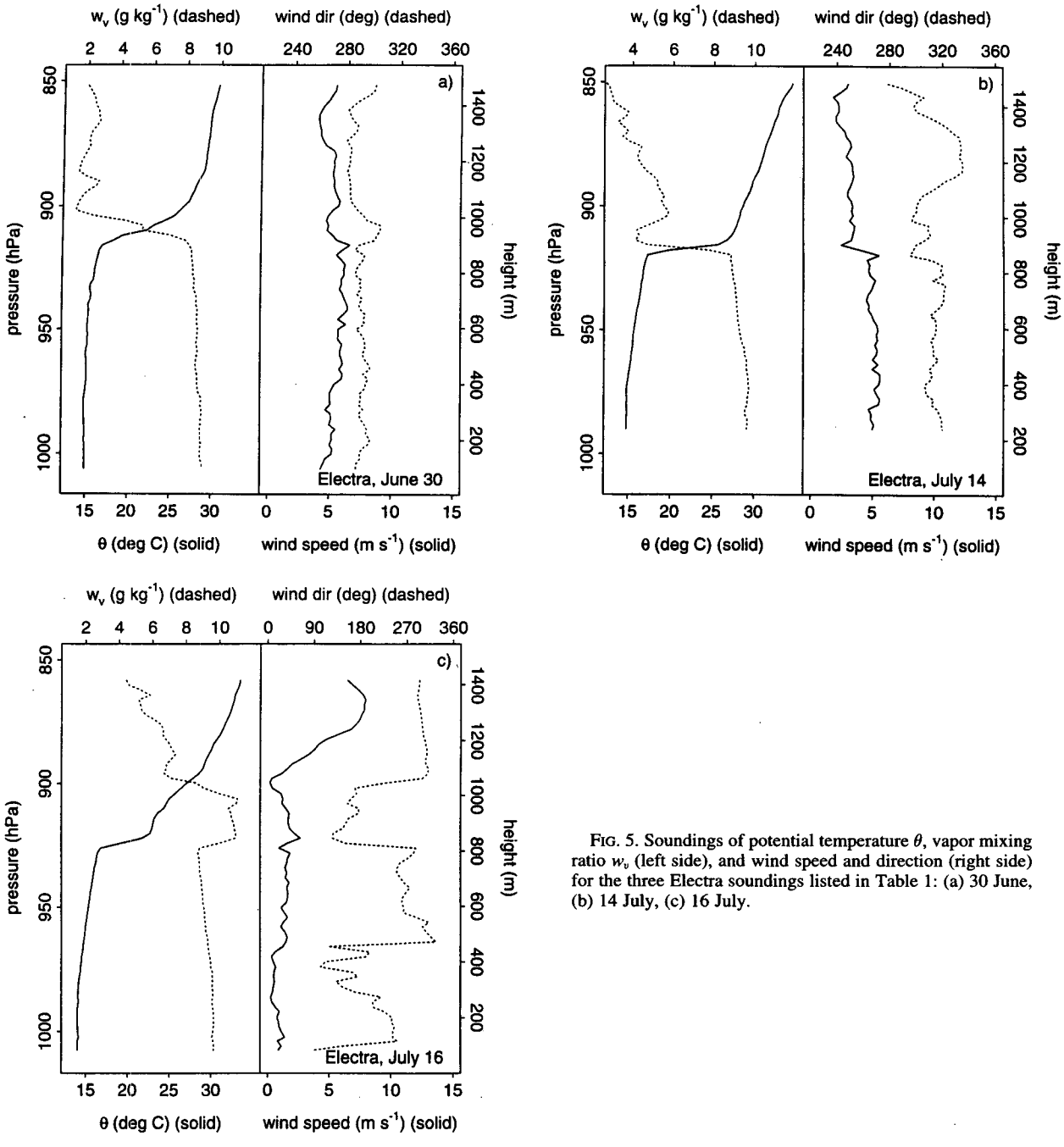

FIG. 5. Soundings of potential temperature θ, vapor mixing ratio w_v (left side), and wind speed and direction (right side) for the three Electra soundings listed in Table 1: (a) 30 June, (b) 14 July, (c) 16 July.

gitude. The filled squares on this image also show the starting and stopping points for leg L2. The sampling strategy on this day emphasized vertical over horizontal resolution, limiting the in-cloud penetrations to less than 50 km; we have extended the leg projection along the line of flight to give a better view of the cloud reflectivity variations in the vicinity of the aircraft. The California coast is visible in the northeast corner of Fig. 3.

b. Cloud soundings

Figure 5 shows soundings of potential temperature, mixing ratio, wind speed, and direction for the three Electra soundings listed in Table 1. The θ, w_v plots for 30 June and 14 July (panels 5a and 5b) and profiles of θ_e (not shown) indicate well-mixed boundary layers beneath dry inversions with light winds (<5 m s^{-1}) and little shear. Other soundings from 14 July show a

slightly stable layer at cloud base typical of daytime decoupling between the cloud and subcloud layers. The 16 July layer is characterized by low winds (1–2 m s^{-1}) and a positive moisture jump at cloud top. This overlying moist layer was seen repeatedly on this day; lack of entrainment drying due to this unusual inversion permitted a thick cloud to form despite small surface moisture fluxes.

In addition to these bulk thermodynamic variables, we present measurements of the drop size distribution from the Electra Particle Measuring Systems (PMS) forward scattering spectrometer and optical array probes (FSSP and 260X), and the C130 FSSP. Probe characteristics and uncertainty estimates are discussed in appendix A. For this experiment, the Electra instruments cover a nonoverlapping radius range. We will refer to the FSSP droplet radius r (measured in 14 bins of width $\Delta r = 1.5$ μm with centers at 1.75 μm $\leq r_i \leq$ 21.25 μm) and the 260X raindrop radius R (measured in 57 bins with width $\Delta R = 5$ μm and centers at 27.5 μm $\leq R_i \leq$ 307.5 μm). The C130 FSSP measured droplets in 15 bins with bin centers at 1.75 μm $\leq r_i \leq$ 22.75 μm; C130 precipitation data are not available for these days. The cloud soundings in Fig. 6 show the following moments of the FSSP size distribution $n(r_i)\Delta r$:

Droplet number: N_r (cm^{-3})

$$N_r = \sum_{i=1}^{14} n(i)\Delta r$$

Droplet volume mean radius: r_{vol} (μm)

$$r_{vol}^3 = \langle r^3 \rangle = \left(\sum_{i=1}^{14} n(i) r_i^3 \Delta r\right)/N_r, \qquad (1)$$

where ρ_w is the density of liquid water and $\langle r^k \rangle$ denotes the kth moment of the number distribution:

Droplet liquid water content q_r: (g m^{-3})

$$q_r = \frac{4}{3}\pi \rho_w N_r r_{vol}^3. \qquad (2)$$

We will also use two vertically integrated measures of the droplet size distribution: the liquid water path LWP (g m^{-2}) and visible wavelength optical depth τ (see, e.g., Nakajima et al. 1991):

$$\text{LWP} = \int_{z_{bot}}^{z_{top}} q_r dz \quad (\text{g m}^{-2}) \qquad (3)$$

$$\tau \approx \frac{3}{2\rho_w}\int_{z_{bot}}^{z_{top}} \frac{q_r}{r_e} dz \approx \frac{3}{2\rho_w}\int_{z_{bot}}^{z_{top}} \frac{q_r}{r_{vol}} dz, \qquad (4)$$

where z_{top} and z_{bot} (m) are the height of cloud top and cloud base, and we have approximated the effective radius ($r_e = \langle r^3 \rangle / \langle r^2 \rangle$) by r_{vol}.

Six vertical soundings of q_r, N_r, and r_{vol} are shown in Fig. 6; the values have been binned in 2-hPa intervals and averaged. In addition to q_r we show JLWC, the cloud liquid water measured with the Johnson–Williams (Cloud Technologies) hot wire probe. Also shown on the graph are estimates of local cloud top and cloud base (marked by ◇ and used to calculate the cloud thickness h in Table 2). On 14 and 16 July, both liquid water probes in the C130 and Electra showed stepped adiabatic liquid water profiles, which we believe are due to variations in cloud-base height over the 20-km horizontal traverse of the sounding. For these cases, we use an upper and a lower adiabat to estimate separate cloud bases marked by a ◇ and a □. It is generally easy to distinguish the actual cloud base from the lower level "scud" seen in Fig. 6d.

We have also determined the range and median of all cloud bases and cloud tops determined by full or partial Electra soundings for the three days. These are marked by the bold vertical line and circle in Figs. 6a,c,e. Although cloud-base heights rise as the layer thins through the course of each flight, we observe variations as large as 170 m in cloud-base height between adjacent soundings (or, as we note above, 100-m variations within the same sounding). A vertical cloud thickness is difficult to estimate due to this horizontal variability, but subtracting cloud-top and cloud-base height pairs taken from each complete sounding gives a median cloud "thickness" of 220 m for 30 June, 333 m for 14 July, and 352 m for 16 July, with a thickness range of ±50% about these medians.

We will need both the measured and adiabatic droplet size and liquid water path to determine initial conditions and parameter ranges for the precipitation models discussed in section 4. The straight, dashed line on the left side of each panel in Fig. 6 shows the adiabatic liquid water content given by

$$q_{adia} = cz \quad (\text{g m}^{-3}), \qquad (5)$$

where $c = 2.3 \times 10^{-3}$ g m^{-3} m^{-1} is appropriate for the range of cloud-base temperatures and pressures found in FIRE.

Inserting (5) into (3) gives the values of adiabatic liquid water path listed in Table 2:

$$\text{LWP}_{adia} \approx 1.15 \times 10^{-3} h^2 \quad (\text{g m}^{-2}), \qquad (6)$$

where h (m) is the cloud thickness between the two ◇ marks on the sounding.

In the right half of each panel in Fig. 6 we show N_r, measured by the FSSP, as well as two estimates of the volume mean radius. The solid line is a plot of r_{vol} using the aircraft-measured N_r and liquid water content (q_r from the corrected FSSP for the Electra, or JLWC, with its consistently higher liquid water concentrations from the C130). The dotted line is a plot of $r_{vol,adia}$, created using N_r from the FSSP and q_{adia} from (5). In a precipitating cloud, in which the droplet concentration is re-

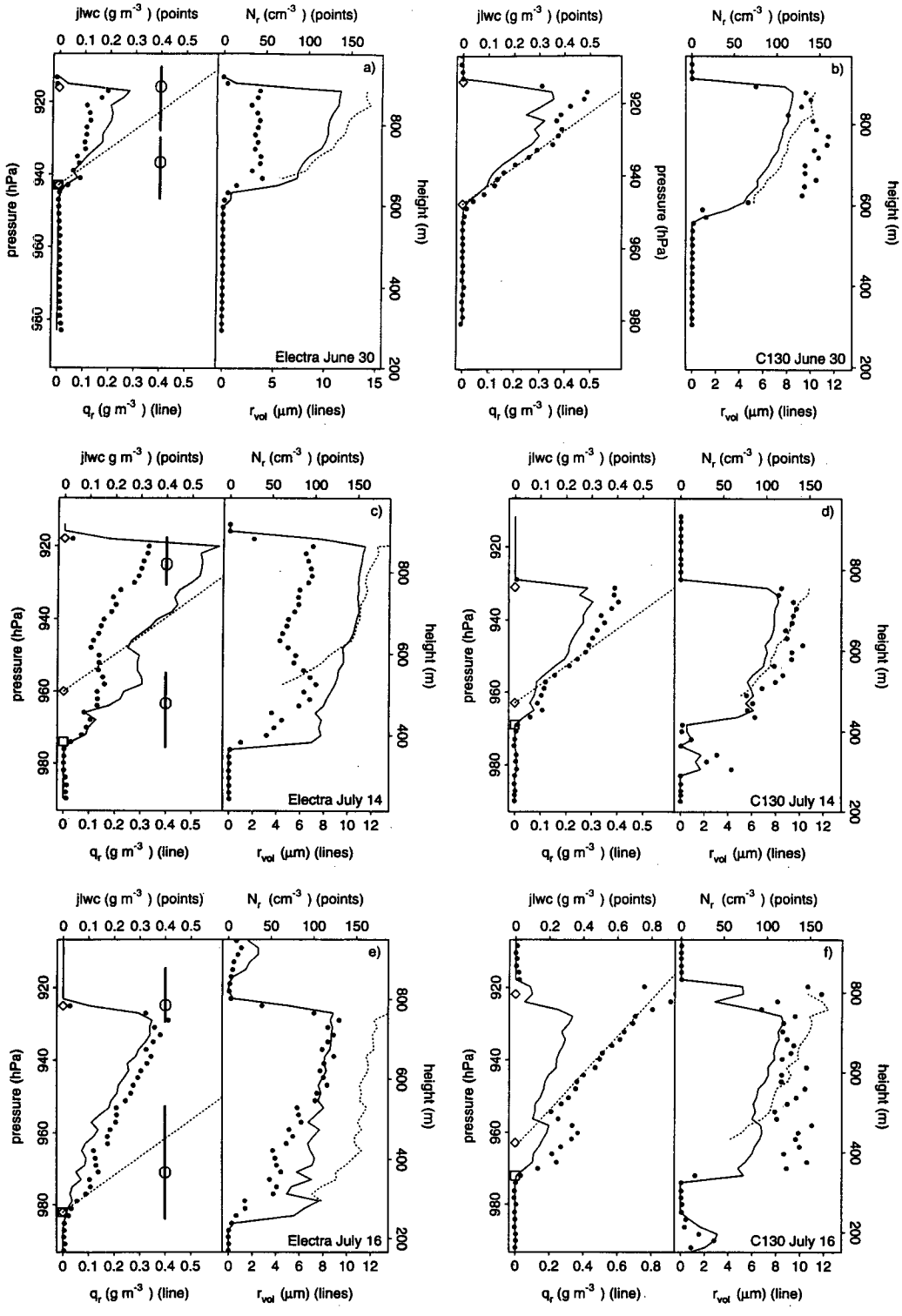

FIG. 6. Cloud liquid water profiles for three pairs of Electra and C130 soundings. FSSP-integrated liquid water content (q_r, left, solid line), adiabatic liquid water content (left, straight dashed line), and the Johnson–Williams liquid water content (JLWC, left, points). The right side of each panel shows the FSSP volume-mean radius (r_{vol}, right, solid line), the adiabatic volume-mean radius (dashed line, right), and the FSSP number concentration (N_r, right, points). The circles and heavy vertical lines on the Electra soundings give the median and range of cloud-base and cloud-top altitudes for the flight's Electra soundings, while the ◇ symbols show the cloud-top and cloud-base heights $z_\diamond$ and the □ denotes a second cloud-base height (see Table 2). (a) 30 June sounding ES, (b) 30 June sounding CS, (c) 14 July sounding ES, (d) 14 July sounding CS, (e) 16 July sounding ES, (f) 16 July sounding CS.

TABLE 2. Cloud thickness h (between $z_\diamond$), measured LWP_{meas}, adiabatic LWP_{adia}, measured τ_{meas}, adiabatic τ_{adia}, and cloud-base height difference ($z_\diamond - z_\square$) for the Electra and C130 soundings of Fig. 6. C130 LWP_{meas} and τ_{meas} use JLWC, Electra uses FSSP q_r.

Sounding	h (m)	LWP_{meas} (g m^{-2})	LWP_{adia} (g m^{-2})	τ_{meas}	τ_{adia}	$z_\diamond - z_\square$ (m)
a) 30 June Electra	234	40	63	6.5	7.6	–
b) 30 June C130	302	84	105	17	17.5	–
c) 14 July Electra	373	146	160	18	21	126
d) 14 July C130	285	56	93	13	15	54
e) 16 July Electra	508	90	297	17	35	–
f) 16 July C130	382	168	167	25	24	72

duced through scavenging, $r_{vol,adia}$ provides an upper limit for the volume mean radius. We integrate (4) to form measured and adiabatic optical depths (τ_{meas} and τ_{adia}) using the r_{vol} and $r_{vol,adia}$ in Fig. 6. Table 2 lists τ_{meas} and τ_{adia} for each sounding.

The results shown in Table 2 and Fig. 6 indicate that 16 July was the thickest cloud layer, but liquid water measurements from the two aircraft give conflicting estimates of liquid water path, which range from near adiabatic to ≈30% of adiabatic for the two C130 instruments. The adiabatic volume mean radius is slightly larger than 12 μm at cloud top. The 14 July layer, although not as thick, is nearly adiabatic, with a maximum value of $r_{vol,adia}$ of 12 μm close to cloud top, but with r_{vol} less than 12 μm throughout the C130 sounding. The 30 June cloud stands in contrast to both 14 and 16 July. The sounding shows an Electra-measured liquid water path less than 60% of that observed on 14 July, and $r_{vol,adia}$ exceeding 12 μm throughout the upper half of the cloud. On both 14 and 16 July the soundings show cloud-base variations of 20%–30% of the cloud thickness and liquid water path.

An upper bound on N_r is provided by the cloud condensation nuclei (CCN) measurements made by the Electra on 30 June and 14 July (Hudson and Frisbie 1991). The 30 June cloud, with low ($N_r \approx 45$ cm^{-3}) droplet concentrations is in clean marine air, with CCN concentrations of ≈75 cm^{-3} at 50 m (leg L0), and mean CCN concentrations at 980 hPa of 50 cm^{-3}. In contrast, the 16 July case, with a maximum N_r of 120 cm^{-3} (Fig. 6e), is more polluted. Hudson and Frisbie report CCN concentrations of 230 cm^{-3} at 1003 hPa (leg L4) with a range for all surface legs of 150–350 cm^{-3}. The higher N_r concentrations observed by the C130 on 30 June (Fig. 6a) ($N_r \approx 150$ cm^{-3}) also appear to be suppressing drizzle in that region. The observers report no precipitation during the C130 30 June flight, although cloud thickness was approximately equal to that observed in the low CCN Electra region, with its larger droplets and substantial precipitation. The different reflectivities in the Electra and C130 regions of Fig. 1 are further evidence for differences in cloud character and air mass in the northern and southern portions of the 30 June scene.

With the exception of the C130 16 July JLWC liquid water measurement (Fig. 6f), the aircraft-measured liquid water contents are subadiabatic. Although both FSSPs show adiabatic liquid water profiles in thin clouds during FIRE, liquid water measurements in thick clouds are difficult to make (Gerber et al., 1993, appendix A), and on these days it is impossible to separate the diabatic impact of precipitation from possible sampling problems. We will assume in section 4 that precipitation is initiated in near-adiabatic clouds, and choose values of q_r, r_{vol}, and N_r that are close to their adiabatic values at midlevel on 14 July.

c. *Precipitation fluxes*

We use the Electra 260X to measure the raindrop number concentration and the precipitation flux, defined by

Raindrop number: N_R (cm^{-3})

$$N_R = \sum_{i=1}^{57} n(i)\Delta R$$

and

Precipitation flux: F_{precip} (mm/day)

$$F_{precip} = 4/3\pi\rho_w \sum_{i=1}^{57} w_T(R_i)R_i^3 n(i)\Delta R, \qquad (7)$$

where $w_T(R_i)$ is the raindrop terminal velocity for bin i. Fall speeds of 10–25-μm drops range from 0.01–0.05 cm s^{-1}, roughly an order of magnitude smaller than the mean updraft velocity of 0.2 m s^{-1}. We expect turbulence to dominate sedimentation in the vertical transport of these droplets (80% of the in-cloud vertical velocities are larger than these terminal fall speeds) and exclude from (7) droplets in the 1–25-μm (FSSP) size range.

1) IN-CLOUD LEGS

Microphysical measurements of F_{precip}, N_R, and the FSSP-derived cloud parameters are shown for horizontal flight legs located 100–150 m below cloud top in Figs. 7, 8, and 9. On 30 June and 14 July drizzle concentrations are large, and across regions of 25–50 km F_{precip} exceed 4–5 mm/day. At these rain rates, in the absence of a vapor flux through the cloud base, a 400-m-thick, adiabatic stratocumulus layer will lose 50% of its liquid water in less than 25 minutes. On 16 July the in-cloud legs were substantially shorter, and were interrupted by an inversion run, so that L1 and L2 are separated by roughly 1 hour. The precipitation flux measured during these brief penetrations is less than 2 mm/day, with N_r roughly half that observed on 30 June and 14 July.

The FSSP-measured r_{vol} and number concentration N_r are shown in panel (b) in each of the Figs. 7–9.

Precipitation scavenging appears to be removing droplet liquid water in all of these clouds. For example, the droplet number concentration plot in Fig. 7b shows a 10-km region of high droplet concentrations, large liquid water content, and low precipitation flux. The peak concentration of $N_r = 80$ cm^{-3} is close to the CCN concentration of 120 cm^{-3} measured by Hudson as the Electra descended to the surface following Leg L7 (Hudson and Frisbie 1991). Averaging over the portions of L7 with $F_{\text{precip}} > 2$ mm/day (20% of the samples) gives a mean droplet concentration in the precipitating cloud of $\overline{N_r} = 31$ cm^{-3}. The average r_{vol} in the precipitating and nonprecipitating regions are approximately equal: $\overline{r_{\text{vol}}} = 10.4$ μm (with $F_{\text{precip}} > 2$ mm/day) compared to $\overline{r_{\text{vol}}} = 10.0$ μm (with $F_{\text{precip}} < 0.5$ mm/day) (27% of the samples).

On 14 July (Fig. 8) the relationship between heavy precipitation, larger values of r_{vol}, and lower values of N_r and q_r is more pronounced. Droplet concentrations are lower, and droplets are larger, in the precipitating regions. For the $\approx$18% of the samples with $F_{\text{precip}} > 2$ mm/day, mean values for (N_r, r_{vol}) are (50.6 cm^{-3}, 10.4 μm), while in the 15% of the samples with $F_{\text{precip}} < 0.5$ mm/day, we find ($\overline{N_r}$, $\overline{r_{\text{vol}}}$) = (83.1 cm^{-3}, 8.8 μm). The larger droplets are consistent with cloud thickness variations similar to those seen in Fig. 6c. If we assume that the regions of highest number concentration for leg L0 ($N_r > 110$ cm^{-3}) are adiabatic, then their mean liquid water content of 0.3 g m^{-3} would indicate a cloud base 130 m below the aircraft. Lowering that cloud base by 100 m would increase the mean r_{vol} at the flight level from 8.6 μm to 10.4 μm [assuming $N_r = 110$ cm^{-3} in (1)]. If this increase in liquid water path and droplet size triggered precipitation, we would expect droplet scavenging to leave regions of larger r_{vol}, lower N_r, and lower q_r, as seen in leg L0. The observation of larger droplet sizes in thinner cloud is also consistent with multichannel satellite retrievals of particle size and optical depth during FIRE, which show an inverse relation between optical depth and effective radius in two precipitating clouds (Nakajima et al. 1991).

The 16 July layer is distinguished from 30 June and 14 July by its moist inversion and by the much lower q_r values seen in legs L1 and L2. These 16 July in-cloud legs (Fig. 9) show peak droplet concentrations of $N_r \approx 110$ cm^{-3}, roughly a third of the 300 cm^{-3} CCN concentration measured by Hudson in a below-cloud sounding immediately following leg L1. The droplet concentration over most of legs L1 and L2 are much lower than this (<40 cm^{-3}), but unlike 30 June and 14 July, the mean droplet radii are also quite small, with $4 < r_{\text{vol}} < 7$ μm during the first half of L2.

Precipitation was also encountered below cloud on each of the days, with horizontal spacing that matches that of the in-cloud precipitation and the satellite reflectivity maxima (Figs. 1 and 2). For number concentrations below 0.05 cm^{-3} the sampling uncertainties for 60-second averages are too large to accurately estimate F_{precip}, but do provide an indication of the presence of drizzle.

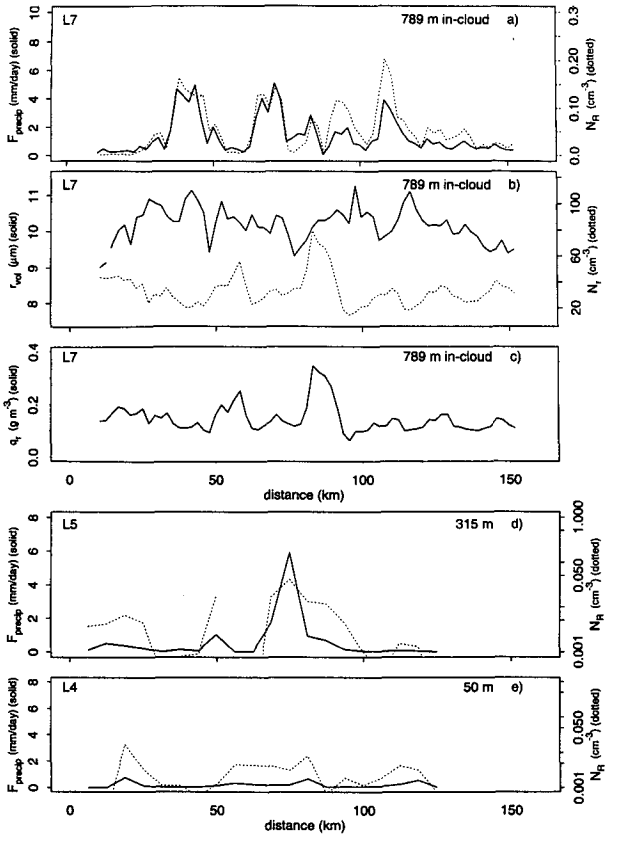

FIG. 7. Aircraft measurements of precipitation microphysics on 30 June. (a) Twenty-second averages of the precipitation flux F_{precip} (solid line) and drop number concentration N_R for raindrops larger than 20 μm (dotted line) during in-cloud leg L7. (b) Cloud droplet (FSSP) volume mean radius r_{vol} (solid line) and number concentration N_r for the same leg. (c) FSSP liquid water content q_r. (d) and (e) Sixty-second averages of F_{precip} and N_R for midlayer flight legs L5 and L4, respectively. Drop number concentrations less than 0.05 cm^{-3} provide only qualitative indications of the presence of raindrops with $R > 20$ μm.

2) WATER FLUXES

We compare these precipitation fluxes with the horizontally averaged vapor fluxes in Fig. 10 for the level legs listed in Table 1. Approximate cloud bases and tops are indicated by the dotted lines; the highest flight level shown in each diagram is typically 100 m below cloud top. The dark squares indicate bulk flux estimates using radiometric measurements of the sea surface temperature (θ_0) taken at 50 meters, using the downward-looking PRT6 radiometer. Assuming saturation at the sea surface [with surface pressure p_{sfc} and saturation vapor mixing ratio $q_{s0}(p_{\text{sfc}}, \theta_0)$] and using the measured horizontal wind speed and vapor mixing ratio V_{50} and q_{v50} at 50 m give for the vapor flux F_{qv}

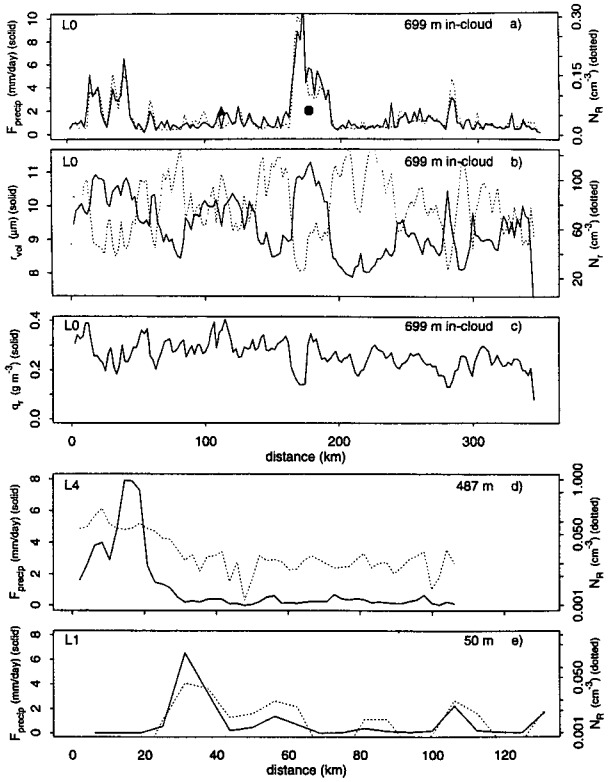

FIG. 8. As in Fig. 7 but for 14 July 1987. (a) Here, F_{precip} and N_R for extended in-cloud leg L0, (b) N_r and r_{vol} for L0, (c) q_r for L0, (d) F_{precip} and N_R for subcloud leg L4 (60-second average), (e) F_{precip} and N_R for surface leg L1 (60-second average). The triangle and circle show the location of the averaged raindrop spectra shown in Fig. 17.

$$F_{qv} = \rho_0 C_D V_{50}(q_{s0} - q_{v50}), \qquad (8)$$

where ρ_0 is the air density and $C_D = 1 \times 10^{-3}$ is the surface transfer coefficient (Boers and Betts 1988).

Two values for the aircraft-measured vapor flux averages are shown in Fig. 10, 2 km high-pass filtered (circles) and unfiltered (triangles). We find on both 30 June and 14 July that variations at scales larger than 2 km make the major contribution to the vapor flux above the surface layer, something also observed by Paluch and Lenschow (1991) on nonprecipitating FIRE days. The flux values near cloud base are uncertain due to both wetting of the Lyman-α and measurement problems with the pressure gust probe (see appendix A), but the surface flux and the cloud-base precipitation flux are each $\approx$1 mm/day for the three days, with (as we have seen) large horizontal variability in the in-cloud precipitation flux on 30 June and 14 July. Precipitation is reaching the surface on 14 and 16 July, but the magnitude of the flux is uncertain due to the low raindrop concentrations measured during the 300-m and 50-m flight legs.

The analysis above neglects the entrainment flux, a potentially important water source or sink. It should act to dry both the 30 June and 14 July layers, and provide water to the 16 July cloud. A typical equilibrium entrainment velocity of 1 cm s^{-1} (see, e.g., Nicholls 1984) acting on the observed 14 July cloud-top moisture decrease of 5 g m^{-3} represents a layer moisture loss equal to the 1 mm/day average cloud-base precipitation flux. We do not have measurements of entrainment velocities for these cases, but the likely presence of entrainment, coupled with the persistence of these clouds, suggests that rainfall cannot be a significant sink for total water in the 30 June and 14 July boundary layers.

Figure 11 gives the vertically averaged precipitation rate from all Electra soundings for the three days as a function of cloud thickness. Figure 11c also shows, for comparison, the sounding averages reported for six days of North Sea stratocumulus observations by Nicholls (1984). Sampling uncertainty is larger for these vertical averages than for the horizontal measurements, both because the available samples are typically less than 20 seconds long and because the averages are taken over vertically and horizontally varying precipitation profiles. It is not surprising, given these caveats, that individual soundings show little correlation be-

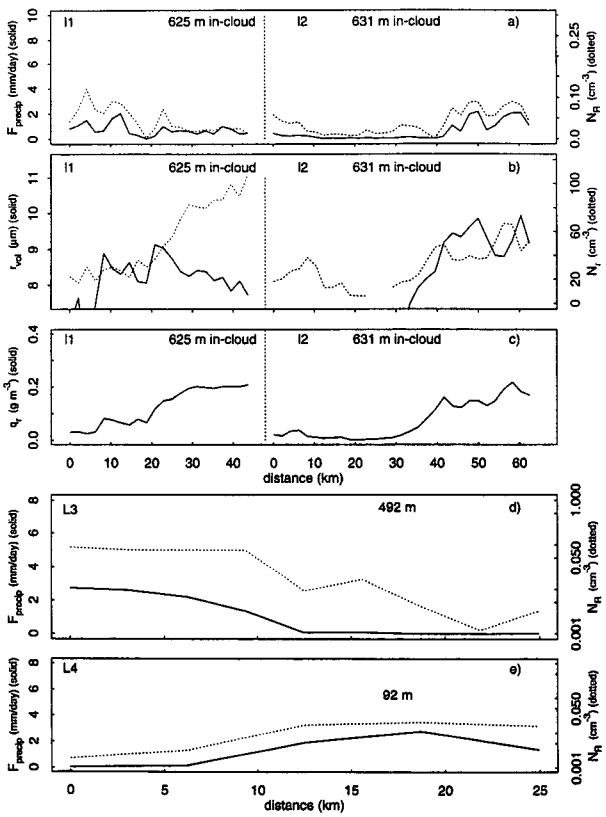

FIG. 9. As in Fig. 7 but for 16 July 1987. (a) Here, F_{precip} and N_R for two in-cloud legs L1 and L2 separated by 60 minutes, (b) N_r and r_{vol} for L1 and L2, (c) q_r for L1 and L2, (d) F_{precip} and N_R for midlayer leg L3 (60-second average), (d) F_{precip} and N_R for leg L4 (90 m) (60-second average).

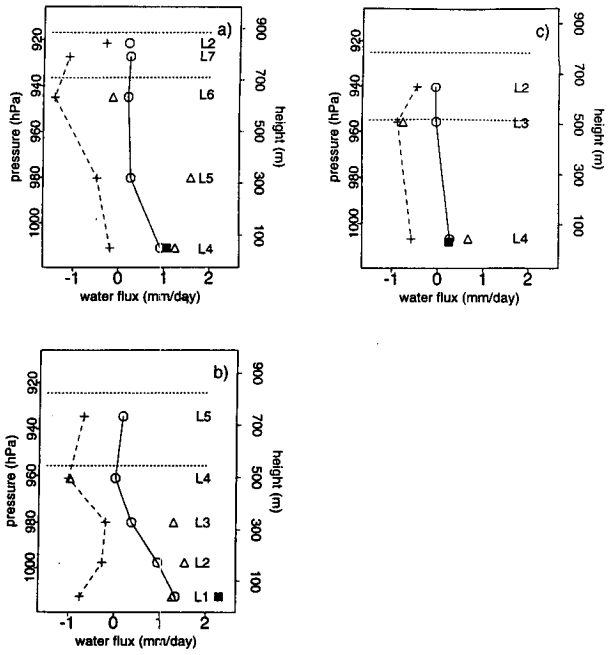

FIG. 10. Horizontally averaged vapor fluxes [(○), 2 km high pass-filtered: (△), unfiltered] and precipitation fluxes (+) for the three cases. Flight legs are listed to the right of each level, and approximate cloud tops and bases are suggested by the dotted lines. The filled squares mark bulk flux estimates using the mean wind speeds and PRT6 radiometric seasurface temperatures for the lowest legs. (a) 30 Jun, (b) 14 Jul, and (c) 16 Jul.

tween cloud thickness and rain rate, although it is clear that the 30 June cloud, despite a mean cloud thickness of ≈200 m, is able to produce drizzle drops in roughly the same concentrations as the 350-m thick 14 July cloud.

3. Satellite observations

We can extend the temporal and spatial range of the cloud measurements through the use of satellite reflectance observations. Figures 1–3 showed VISSR and AVHRR-measured reflectances for the cloud region surrounding the aircraft. We use the National Meteorological Center 1000-hPa windfields to compute the advected trajectory of 256 × 256 km cloud boxes (see Pincus et al. 1992 for details) and retrieve IR and visible band VISSR images for these advected regions at half-hourly intervals, with start and stop times bracketing the aircraft observation period. We use ISCCP calibrations (Desormeaux et al. 1993) to convert satellite instrument counts to outgoing radiance, then infer the cloud optical depth from a radiance lookup table calculated for a range of solar zenith and satellite view angles (see, e.g., Minnis et al. 1992). The uncertainty in the optical depth estimates is about 15%–20% (Rossow et al. 1989). On 16 July the trajectory is close to the coast and the flow onshore. We have ignored those sections of each 16 July image over land (between 25% and 35% of the image area) so that the number of pixels along this trajectory decreases with time.

Figure 12 shows the temporal evolution of the first, second, and third quartiles of the optical depth distributions, where the respective quartiles are those optical depths larger than 25%, 50%, and 75% of the optical depths on each image. The image series are for 30 June (centered on the Electra flight track), 14 July, and 16 July, with the times of various events from Table 1 indicated on the upper axis. The satellite observations can give some indication of how well the small number of available aircraft soundings represent regional cloud conditions, within the uncertainties in both the optical depth and in situ liquid water measurements. We see, for example, that the median optical depth estimated by the satellite at 11:45 PST on 30 June is higher than the Table 2 value of $\tau_{meas} = 6.5$ made during the contemporaneous Electra sounding ES. The 16 July Electra soundings (Fig. 6e and Fig. 9) showed subadiabatic cloud liquid water profiles with $\tau_{meas} \approx 17$, consistent with the satellite-derived median optical depths. In contrast, the optical depth inferred from the C130 JLWC measurements on this day ($\tau_{meas} \approx \tau_{adia} \approx 25$) is greater than that inferred from 83% of the pixels observed by the satellite at the time of the sounding. The 14 July soundings appear to be taken in thinner than average clouds; the τ_{meas} values in Table 2 fall in the lowest 30% of the optical depth distribution retrieved from the satellite measurements.

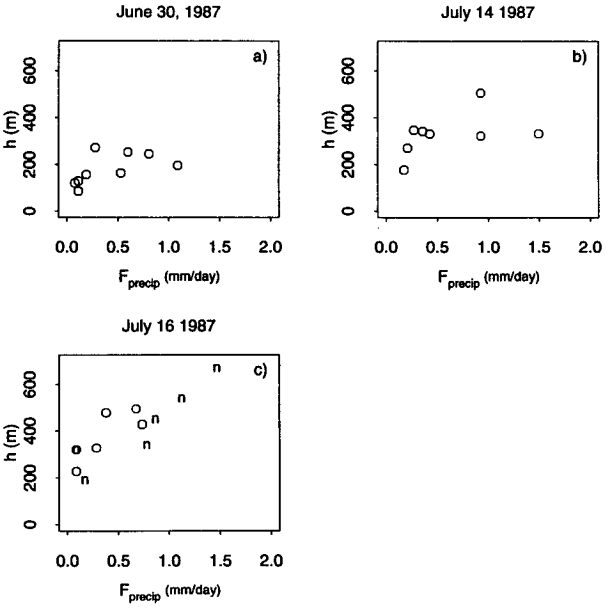

FIG. 11. Average rain rate (mm/day) as a function of cloud thickness for all complete vertical soundings. The average soundings from five North Atlantic flights (marked "n") (Nicholls 1984) are overlaid on the 16 July plot (c) for comparison.

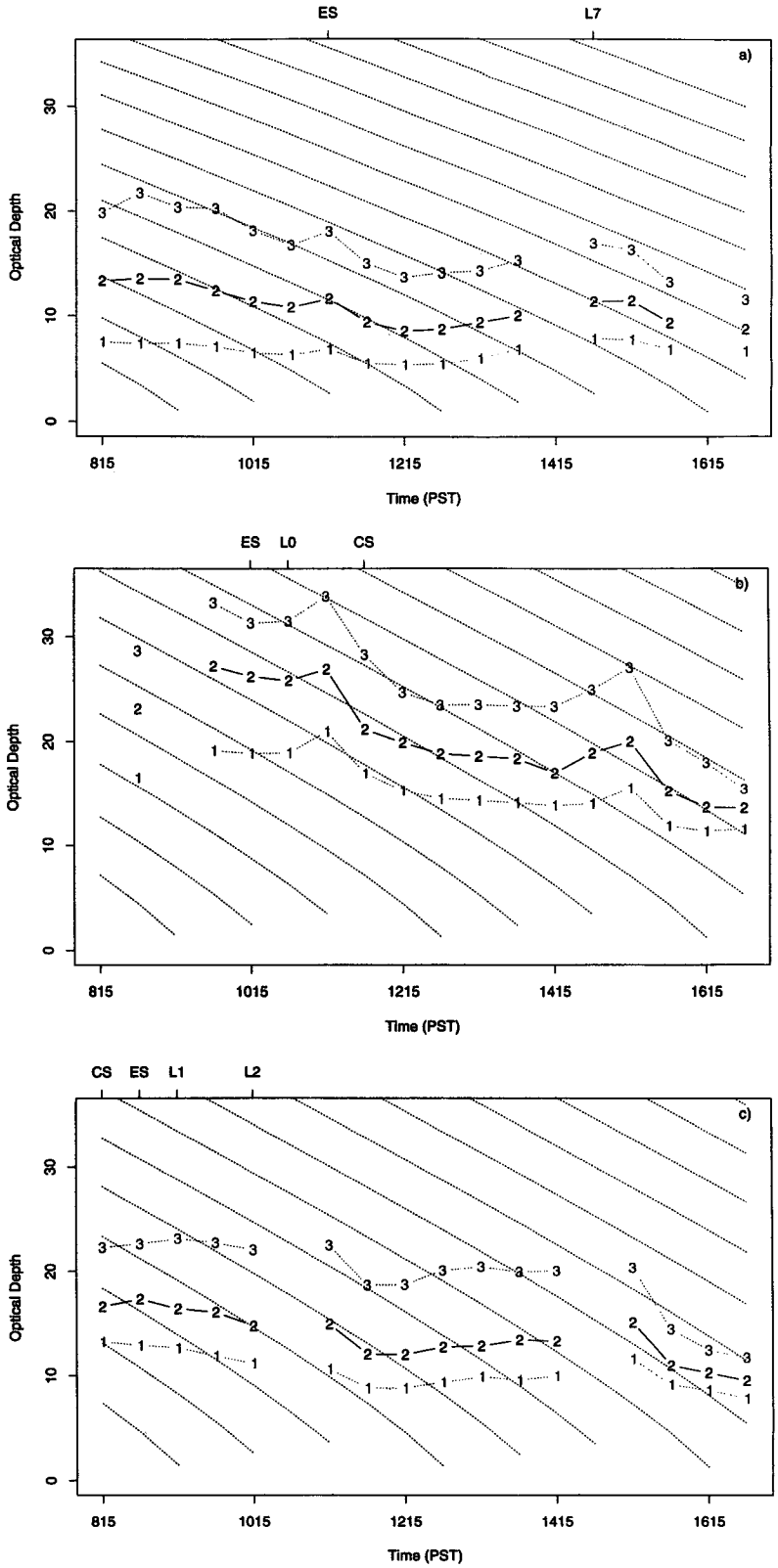

FIG. 12. Cloud optical depth for fully cloudy pixels ($R > 0.20$) on (a) 30 June, (b) 14 July, and (c) 16 July. The lines labeled 1, 2, and 3 give the first, second, and third quartiles. Dashed lines show the expected decrease in τ given a net water loss of 1 mm/day, assuming $\beta = 1$ and $N_r = 50$ cm^{-3} (30 June), $N_r = 110$ cm^{-3} (14 July), and $N_r = 120$ cm^{-3} (16 July).

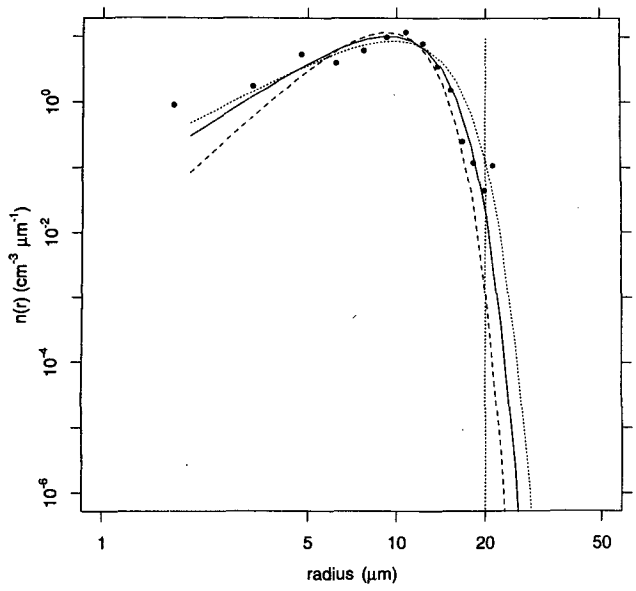

FIG. 13. Points represent 60-second average FSSP spectrum from 14 July leg L0 (18:26 UCT). Solid line represents fit to the distribution using the gamma distribution of (12) with $N_0 = 75$ cm^{-3}, $r_{vol} = 10.5$ μm, var$r = 0.11$, $\nu = 0.3$. Long dashed line shows gamma distribution with $r_{vol} = 10$ μm, var$r = 0.08$, $\nu = 0.7$, $N_0 = 75$ cm^{-3}. Dotted line shows gamma distribution with $r_{vol} = 11$ μm, var$r = 0.13$, $\nu = 0.1$, $N_0 = 75$ cm^{-3}.

We can estimate the impact of changes in cloud thickness on the optical depth by substituting (5) into (4):

$$\tau \approx 2.4 \times 10^{-4} N_r^{1/3} \beta^{2/3} h^{5/3}, \qquad (9)$$

where $0 < \beta \leq 1$, a measure of subadiabaticity, is the ratio of the actual to the adiabatic liquid water content (β assumed constant through the cloud layer), and h and N_r are measured in units of m and cm^{-3}, respectively. If we evaluate this equation for the conditions during the Electra sounding on 14 July ($\beta \approx 1$ and $N_r = 100$ cm^{-3}), we find that the median optical thickness at the time of the Electra sounding ES ($\tau \approx 26$) corresponds to a cloud thickness of $h \approx 415$ m, within the range of the observed cloud-base variability. We conclude that much of the 14 July cloud was thicker than the 333-m median value inferred from all aircraft soundings in section 2.

We measure optical depth changes in Fig. 12: the slightly curved dashed lines in the figure indicate the rate of change in optical depth calculated using (9), assuming N_r constant at the values given in the caption, and a constant net loss of liquid water equivalent to a 1 mm/day rain rate. Although precipitation rates exceeding 2 mm/day had a significant local impact on droplet number and cloud liquid water, and drizzle was observed in cloud soundings throughout these three days, the median optical depths stay relatively constant over the mesoscale-sized regions. In addition, the cloud fraction (estimated with a variable reflectance threshold, but not shown) remains above 95% over the course of each day, in contrast to the predictions of Albrecht (1989), who suggested a more sensitive dependence of cloud fraction on precipitation amount.

All three days show their greatest optical depth fluctuations at roughly 11:15 and 15:15 PST, with approximately constant values before each fluctuation. It is difficult to say without a larger sample whether the near-identical timing of these transitions and steady periods is coincidental. The afternoon decrease appears in other nonprecipitating FIRE clouds, and corresponds in time to the solar-heating-induced afternoon cloud minimum seen in satellite and rawinsonde observations (see, e.g., Betts 1990). The morning fluctuations (which are not accompanied by changes in cloud fraction or cloud-top temperature) are largest for the brightest pixels. We would expect these thicker clouds to have the highest precipitation and entrainment rates as well as the strongest solar absorption.

4. Models of raindrop growth: Autoconversion and accretion

The aircraft and satellite observations of sections 2 and 3 present precipitation patterns that indicate large local depletion of cloud liquid water, although these large local changes are not reflected in the regional estimates of optical depth. The observations also indicate that the 30 June cloud, formed in clean marine air, can generate precipitation fluxes as large as the 14 July layer, although the median thicknesses of the two layers give adiabatic liquid water paths that differ by more than a factor of 2. In this section we consider the sensitivity of rain rate to the cloud droplet distribution and cloud thickness, using equilibrium calculations with models that include the effects of turbulence, coalescence, sedimentation, and condensation.

In section 4a we focus on the production of small drizzle drops through the collision of condensation-produced cloud droplets, and show that typical marine stratocumulus droplet distributions, with their low liquid water concentrations and small volume mean radii, evolve through coalescence much more slowly than representative distributions from precipitating cumulus clouds. In section 4b we consider how measurable precipitation can be produced given the low autoconversion rates typical for stratocumulus. In that section we review Baker's analytic model and introduce a one-dimensional equilibrium model patterned on Nicholls's work.

a. *Autoconversion*

A 200-m thick adiabatic cloud with a constant droplet concentration of 50 cm^{-3} will have drop size distributions with volume mean droplet radii between 5 and 12 μm. Autoconversion is the process by which these

products of condensation growth collide and produce larger raindrops; the raindrops can then accrete cloud droplets and form precipitation.

We can directly estimate the autoconversion rate by calculating the rate of mass transfer past an arbitrary droplet size for a particular cloud droplet distribution using the stochastic collection equation (e.g., Berry and Reinhardt 1974a):

$$\frac{\partial n(x)}{\partial t} = \int_0^{x/2} n(x_c)n(x')K(x_c, x')dx' - \int_0^{\infty} n(x)n(x')K(x, x')dx'. \quad (10)$$

Here the number concentration in the mass range $x \rightarrow x + dx$ is $n(x)dx$ (cm^{-3}), and collisions that produce raindrops of mass x occur between droplets of mass x' and $x_c = x - x'$. The collection kernel K depends on the collision efficiency E (in the range $0 \rightarrow 1$) and the differential fall velocity $\Delta V(x, x') = V(x) - V(x')$:

$$K(x, x') = \pi r^2 E(x, x')\Delta V(x, x'), \quad (11)$$

where we have used $4/3\pi\rho_w r^3 = x$.

We have tested the sensitivity of the results discussed in this section and section 4b(2) to three choices of hydrodynamic kernel, using the collection efficiencies of Hocking and Jonas (1970) and Davis and Sartor (1967) [used by Reinhardt (1972)], a combination of the kernels of de Almedia (1977) and Hall (1980), and Jonas and Mason (1974) (used by Nicholls 1987). Variations in the coalescence kernel change the autoconversion rates and equilibrium precipitation fluxes reported below by ≈10%–20%.

We use droplet mass distributions of the form

$$n(x) = N_0 x_f^{-1}(1 + \nu)^{(1+\nu)}/\Gamma(\nu + 1)\left(\frac{x}{x_f}\right)^{\nu} \times \exp\left[-(1 + \nu)\frac{x}{x_f}\right]. \quad (12)$$

Here N_0 (m^{-3}) is the total number concentration, and the first moment of the mass distribution x_f (with corresponding radius r_{vol}) is

$$x_f = \langle x \rangle = \int_0^{\infty} xn(x)dx; \quad r_{\text{vol}} \propto x_f^{1/3}. \quad (13)$$

For these distributions the parameter ν is related to the relative variance in the mass and the radius, var$x$ and var$r$, by (Berry and Reinhardt 1974a)

$$\text{var}x = \frac{\langle\langle x^2\rangle - \langle x\rangle^2\rangle}{\langle x\rangle^2} = 1/(1 + \nu) \approx 7.14\ \text{var}r. \quad (14)$$

Figure 13 shows a fit to the Electra FSSP observations using (12). It is a 60-second average FSSP spectrum taken on 14 July leg L0 in a region of moderate precipitation. The solid line is a fit through the data with ν chosen to match the distribution mass variance of var$x$ = 0.77, var$r$ = 0.11, the volume mean radius r_{vol} = 10.5 μm, and total number concentration of N_0 = 75 cm^{-3}. Liquid water content for this choice of parameters is q_r = 0.36 gm^{-3}. Also shown are two other curves typical of distribution parameters observed in the middle of these clouds. We have examined 100 30-second-averaged midcloud droplet spectra for precipitating regions of the 30 June and 14 July clouds and found r_{vol} between 10 μm and 12 μm with relative radius variances var$r$ between 0.04 and 0.12 (ν between 2.2 and 0.2). In examples throughout this section we will use three distributions that approximately represent adiabatic spectra in the middle of the 30 June and 14 July clouds: the fit to Fig. 13 (which we will call Γ_1), Γ_2 = (r_{vol} = 10.5 μm, N_0 = 100 cm^{-3}, q_r = 0.48 g m^{-3}), and Γ_3 = (r_{vol} = 11.5 μm, N_0 = 75 cm^{-3}, q_r = 0.48 g m^{-3}).

Using (10) and the algorithm of Berry and Reinhardt (1974a) we can calculate the autoconversion rate A, defined here as the time rate of change of the distribution mass below 20 microns:

$$A\ (\text{kg m}^{-3}\ \text{s}^{-1}) = -\frac{dq_r}{dt} = +\frac{dq_R}{dt} = -\frac{d}{dt}\int_0^{x_0} xn(x)dx, \quad (15)$$

where we have used q_r and q_R to represent the liquid water content in the cloud droplets and raindrops, respectively, and written the mass of 20 μm raindrops as x_0. The numerical scheme is able to integrate (10) with a mass loss of ≈0.1% over 4 hours, using a 2-second time step and a constant collection kernel. Analytic solutions to (10) have been found for both the constant kernel and a kernel proportional to the sum of the drop–droplet masses (Scott 1968). Comparison between the numerical and analytic solutions for these two kernels show concentration errors of less than 1% for 200-μm raindrops after 60 minutes of integration.

The choice of 20 μm for the autoconversion boundary is somewhat arbitrary and can be moved to slightly smaller sizes (18–19 μm) without qualitatively changing the results presented below. In section 4b we discuss a model in which the droplet population below the autoconversion boundary will be specified using a fit to observations. Removing this boundary, or moving it to significantly smaller sizes, requires an accurate treatment of the processes determining the breadth of the number distribution, and introduces the complicating effects of the aerosol distribution, entrainment, and evaporation. There is currently no agreement on the relative role played by each of these processes in determining the droplet distribution shape (see, e.g., Cooper 1989). Rather than attempt to predict both the droplet distribution in the FSSP size range and the distri-

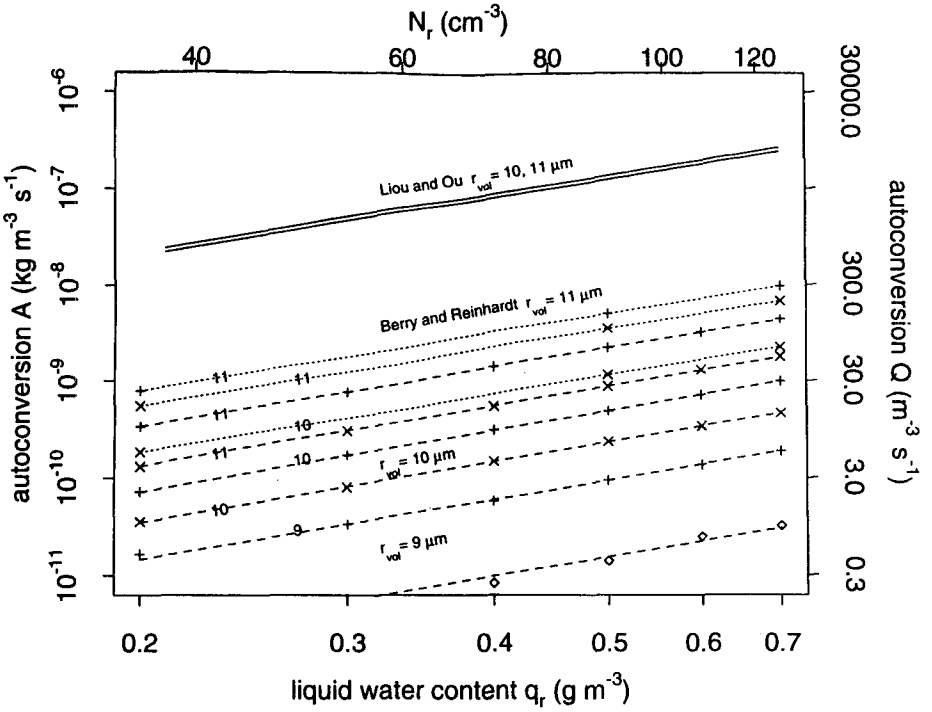

FIG. 14. Autoconversion rate A as a function of q_r (bottom axis) and N_R (assuming $r_{vol} = 11$ μm, top axis). Solid lines show the parameterization of Liou and Ou for $r = 10$ μm, $r_{vol} = 11$ μm; dotted lines show the parameterization of Berry and Reinhardt for $r_{vol} = 11$ μm; dashed lines show least-squares fits to the explicit A calculated for $r_{vol} = (9, 10, 11$ μm). Each radius case (except for Liou and Ou) is calculated with two values of varr: (+) varr = 0.11, (×) varr = 0.08, and for $r_{vol} = 9$ μm, (◇) varr = 0.09. The right axis shows the particle production rate Q given A, assuming a drop radius $R_0 = 20$ μm.

bution of larger raindrops, we will focus on the way in which a given small droplet distribution produces an equilibrium precipitation spectrum in section 4b. We integrate (10) using 60 logarithmically spaced bins between 2- and 1800-μm radius, with bin centers at 16, 18, 20.2, and 22.6 μm in categories 19–22, so that we specify droplet concentrations for $r \leq 19$ μm and let these droplets supply new precipitation particles through both coalescence and condensation growth to bins 21 and above.

Our definition of autoconversion differs from that introduced by Berry and Reinhardt (Berry and Reinhardt 1973; Berry and Reinhardt 1974b; Richard and Chaumerliac 1989). They began with an initial distribution specified by (12) and let it evolve by coalescence. Using eight different distributions with values of $r_{vol} = (10, 12, 14, 16)$ μm, $\nu = (0, 3)$, and $q_r = 1$ g m^{-3}, they measured the time T_2 required for the mass-weighted mean R_g to reach 50 μm, where R_g is defined as

$$R_g^3 = \int_0^\infty x^2 n(x)dx \Big/ \int_0^\infty xn(x)dx. \qquad (16)$$

Typically this requires T_2 between 6 and 25 minutes. At the end of this time the original distribution has evolved into a bimodal spectrum with a new drizzle mode (which they called "S2") containing liquid water content L_2. The autoconversion rate is then given by

$$A = L_2/T_2. \qquad (17)$$

It is scaled to other liquid water contents q_r by the observation, based on a set of 30 model runs, that $q_r T_2 \approx$ constant.

Marine droplet size distributions, with $r_{vol} = 10$–12 μm and $q_r \approx 0.4$ g m^{-3}, can have values of T_2 exceeding 90 minutes, with most of the spectral evolution occurring after 75–80 minutes have elapsed. Under these conditions, L_2/T_2 is dominated by the collection due to the new population of 30–50-μm raindrops in the evolved spectrum, and is related to, but overestimates, the "instantaneous" rate at which the initial gamma distribution can generate raindrops larger than 20 μm. We find in our integrations that the mass transfer rate over the first 5–10 minutes of spectral evolution is nearly constant; we use that value for the autoconversion A.

We compare the two approaches in Fig. 14. We show our autoconversion rate (long dashed line) as a function of q_r, for $r_{vol} = (9, 10, 11)$ μm and two relative variances. All lines have a slope of 2 ($A \propto N_r^2$), in

agreement with the autoconversion rate estimated by continuous collection for a population of N_r (cm^{-3}) droplets of mass M and radius r collecting similar cloud droplets with constant efficiency E_c:

$$A = N_r \frac{dM}{dt} = E_c \pi r^2 N_r^2 M \Delta V. \quad (18)$$

As expected, our autoconversion rates are qualitatively similar to, but lower than, those of Berry and Reinhardt (by a factor of 2 for $r_{vol} = 11$ μm, $\nu = 0.3$) and are also more sensitive to the distribution variance. Figure 14 also shows a parameterization from Liou and Ou (1989) (following Chen and Cotton 1987) (solid lines). The Liou and Ou parameterization uses (18) with a collection efficiency of $E_c = 0.55$, $N = N_r$, and ΔV taken as the fall speed for cloud droplets smaller than 20 μm. With these parameter values (18) gives autoconversion rates that are about 2.5 orders of magnitude greater than Berry and Reinhardt, and 3.2 orders of magnitude greater than (15) for 10-μm drops with $\nu = 0.7$. Substituting the de Almedia/Hall kernel for the Jonas and Hocking kernel increases our autoconversion rate slightly (by $\approx$10–30%).

The rapid autoconversion predicted by (18) is due to the choice of $E_c = 0.55$, which is appropriate for a drop size distribution in which precipitation has already formed. Figure 15 shows the collection efficiency for three different droplet sizes as a function of collector size (Jonas and Hocking kernel). For collector drops below 25 μm, the mean collection efficiency falls rapidly below 0.10 and is typically below 0.05 for the Γ distributions used here.

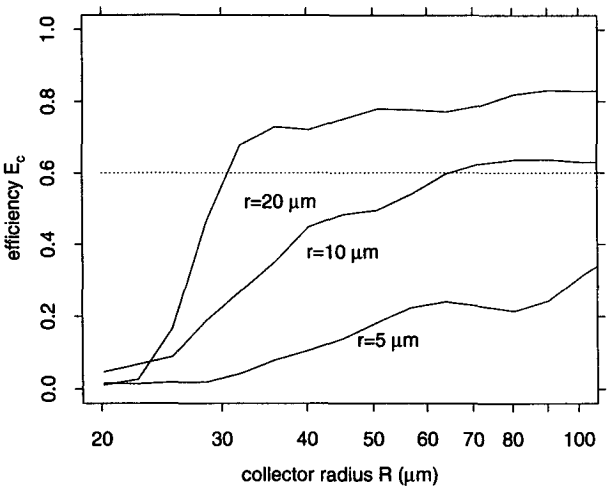

FIG. 15. Collection efficiency as a function of collector drop radius for three cloud droplet sizes. Dotted line shows constant efficiency $E_c = 0.6$.

b. *Accretion growth: Impact of sedimentation and turbulent transport*

Nicholls (1987) proposed that turbulence played a crucial role in stratocumulus precipitation, keeping small drizzle drops in circulation long enough to grow by coalescence. His model used a nonlocal turbulence closure [the "integral equation" closure of Pasquil and Smith (1983)] to move air parcels between vertical levels, with the probability that a parcel would make a transition from level i to level j determined by an observed vertical velocity distribution. This one-dimensional framework allows detailed, time dependent, microphysical calculations to be carried out relatively quickly (Nicholls used 49 size classes). Unlike a higher-order closure scheme, this nonlocal closure moves individual cloud parcels between vertical levels, so that a parcel-specific supersaturation can be diagnosed for droplet condensation growth, and the impact of sedimentation and coalescence on the parcel can be calculated during the movement between levels. The model turbulent velocity field is specified throughout the calculation, however, so microphysical changes are unable to influence layer dynamics.

Below we adopt Nicholls's approach, substituting for the integral equation closure a similar, nonlocal scheme due to Stull (1984). In Stull's closure, the "transilient" matrix $c_{ij}(\Delta t)$ represents the portion of air mixed into the level at height z_i from the level at height z_j during a time step of length Δt, and plays the role of the transition matrix in Nicholls's model. Calculating turbulent transport using Nicholls's transition matrix requires the iterative use of all raindrop concentration profiles for 10 previous time steps. Stull's technique is more highly parameterized but much easier to implement, with absolute mass conservation and boundary conditions that are easily specified. The connection between the transilient matrix and an observed velocity profile is more tenuous, but the transilient model requires an order of magnitude less computer time than the integral equation closure to converge to steady-state precipitation profiles. The derivation of the transilient matrix for the model described below is discussed in appendix B.

Recently, Baker (1993) proposed an analytic version of Nicholls's model. She replaced the nonlocal turbulence closure with a stochastic diffusion equation for a turbulent plume of sedimenting raindrops, specified a production rate for the smallest raindrops, and let the diffusing drops grow by accretion with a time constant determined from q_r and their size-dependent fall speed. The resulting equilibrium precipitation rate can be represented in closed form, which is extremely attractive for precipitation parameterizations in large-scale models. In section 4b(1) we describe the analytic model and calculate equilibrium raindrop distributions for conditions approximating those of section 2. In section 4b(2) we compare the analytic solutions to explicit coalescence calculations using the transilient model.

1) THE IMPACT OF TURBULENCE: THE ANALYTIC EQUILIBRIUM CALCULATION

The analytic model traces the time evolution of a plume of precipitation particles of radius $R(t)$ as they fall and accrete cloud droplets. Their fall speed $V(R)$ is modified by the turbulent vertical velocity w', which is assumed to have a Lagrangian autocorrelation function of the form

$$\overline{w'(t)w'(t')} = \sigma_w^2 \exp(-|t - t'|/\tau_w), \quad (19)$$

where the overbar represents a spatial average, σ_w^2 is the variance of the vertical velocity ($0.2 \leq \sigma_w \leq 0.4$ m s^{-1} for these three days), and τ_w is the Lagrangian timescale. The Lagrangian timescale can be estimated by $\tau_w = L/\sigma_w$, where L (m) is the turbulence integral length scale (Baker 1993). We find $400 < \tau_w < 1000$ s for our three FIRE cases.

We will write the probability of finding a raindrop that originated from a layer at height z' and finds itself at height z at time t as $F(z, z', t)dz'$. Here F obeys the conservation equation:

$$(w - V(R(t)))\frac{\partial F(z,z',t)}{\partial z} + \frac{\partial F(z,z',t)}{\partial t} = 0. \quad (20)$$

The accretion growth of these falling raindrops can be approximated by a continuous collection equation similar to (18). Assuming that the precipitation particles of radius R fall through a stationary population of small droplets at speed $V = JR$, and that the collection efficiency is a constant E_c, Baker approximates the raindrop growth by

$$R = R_0 \exp\left(\frac{t}{\tau_c}\right), \quad \text{where} \quad \tau_c = \frac{4\rho_w}{\rho_{\text{air}} q_r J E_c}, \quad (21)$$

where ρ_{air} is the dry air density. Taking $J = 8630$ s^{-1} (Johnson 1982), $E_c = 0.6$, and $q_r = 0.48$ g m^{-3} (our distribution Γ_2) gives $\tau_c = 26.8$ min. Thus, raindrop growth from 20 μm to 150 μm requires roughly 54 minutes compared with the 14–18 minutes required for a 50 μm drop to sediment out of a 300-m thick cloud.

With these assumptions, (20) can be solved for a point source at z':

$$F(z, z'; 0) = \delta(z - z'). \quad (22)$$

The magnitude of the raindrop source is given by the autoconversion rate A. We will transform A as in Fig. 16, assuming that all of the liquid water mass goes into raindrops with $R_0 = 20$ μm, and write:

$$Q = \frac{A}{(4\pi R_0^3 \rho_w/3)}.$$

With this assumption the *arrival rate* $S'(z, z'; t)dz'$ (m^{-3} s^{-1}) (i.e., the rate at which raindrops from the spreading plume that originated at height z' arrive at height z) is

$$S'(z, z', t)dz' = F(z, z', t)dz'Q. \quad (23)$$

We can take the Fourier transform of (20), ensemble average over all realizations of the stochastic variable w, and invert to find S'. Integrating this over the thickness h of the cloud layer gives the total average arrival rate (Baker 1993):

$$\bar{S}(z; t) = \int_0^h \overline{S'}(z, z'; t)dz'$$
$$= \frac{1}{2}Q\left(\text{erf}\left[-\frac{z - \Delta z(t)}{\sqrt{2}\sigma_z(t)}\right] - \text{erf}\left[-\frac{z - \Delta z(t) - h}{\sqrt{2}\sigma_z(t)}\right]\right), \quad (24)$$

where the overbar denotes the ensemble average, $\Delta z(t) = \int_0^t V(R(t'))dt' = \int_0^t JR(t')dt'$ is the distance fallen by the plume center, and $\sigma_z(t) = f(t; \tau_l, \sigma_w)$ is the standard deviation of the plume, which is given approximately by Taylor's theorem [see (B4)].

The solid lines in Fig. 16 show the time evolution of $\bar{S}(z, t)$ given a 500-m-thick cloud layer with constant A and turbulence parameters inferred from vertical velocity spectra for the 14 July cloud: $\sigma_w = 0.4$ m s^{-1} and $\tau_w = 450$ s^{-1}. The precipitation particles, initially at radius R_0, are accreting as they fall, with a growth rate given by (21). We have assumed $q_r = 0.48$ g m^{-3}, $E_c = 0.6$, and $\tau_c = 26.8$ minutes. The sensitivity of the precipitation distribution to choices of E_c and h will be discussed in section 5. We show the rate of change of plume concentration at 12.5 minutes (when the raindrops arriving at height z have grown by accretion to $R = 32$ μm) and at 50 minutes ($R = 129$ μm). Figure 16 shows that at a height of 500 m there are on average ≈ 20 m^{-3} raindrops arriving each second. They originated from the layer between 500 and 1000 m, 12.5 minutes previously, and have grown to 32 μm as they have diffused toward $z = 500$ m.

Providing the source rate Q remains constant, we can determine the equilibrium raindrop distribution at height z by transforming $\bar{S}$ to the distribution η (m^{-3} μm^{-1}):

$$\eta(z, R)dR = \bar{S}(z, t)dt \Rightarrow$$
$$\eta(z, R) = \frac{Q\tau_c}{2R}\left(\text{erf}\left[-\frac{z - \Delta z(t_*)}{\sqrt{2}\sigma_z(t_*)}\right] - \text{erf}\left[-\frac{z - \Delta z(t_*) - h}{\sqrt{2}\sigma_z(t_*)}\right]\right), \quad (25)$$

where $t_* = \tau_c \ln(R/R_0)$.

Equation (25) predicts the equilibrium raindrop size distribution as a function of height within the cloud, cloud thickness, droplet liquid water content, droplet autoconversion rate, and the turbulence parameters σ_w and τ_w. Baker (1993) finds that the precipitation flux predicted by (25) varies by an order of magnitude as

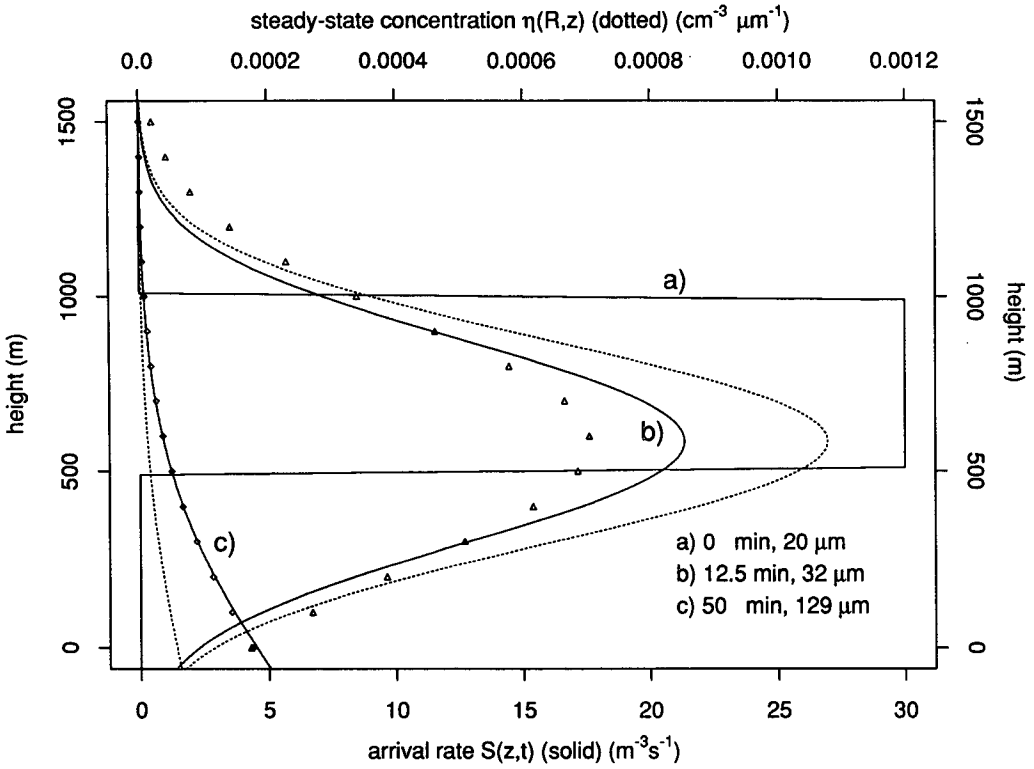

FIG. 16. Solid lines: Total average arrival rate $\bar{S}(z, t)$ of raindrops as given by (24), with an autoconversion rate $A = 10^{-9}$ kg m^{-3} s^{-1} ($Q = 30$ m^{-3} s^{-1}) in a 500-m thick layer at times $t = 0$ min (a), $t = 12.5$ min (b), and $t = 50$ min (c). Dotted lines: The steady-state droplet concentration $\eta(R, z)$ from (25) (upper axis). The symbols (△, ◇) give numerical model results (see section 4b). Plume turbulence parameters are $\sigma_w = 0.4$ and $\tau_w = 450$ s.

(τ_w, σ_w) vary in the range $0.3 < \sigma_w < 0.6$ m s^{-1}, and $300 < \tau_w < 900$ s. Below we will fix (τ_w, σ_w) to their 14 July values and focus on the sensitivity of the precipitation rate to changes in cloud microphysics.

The dotted lines on Fig. 16 (values on the top axis) give contours of $\eta(z, R)$ for $R = 32$ and 129 μm. We might expect η to overestimate the rain rate because modeled raindrops continue to grow by accretion as they diffuse above the 1000-m "cloud top" in Fig. 16, effectively seeding the upper cloud with small concentrations of raindrops.

Choosing autoconversion rates in the range suggested by Fig. 14, a cloud thickness of $h = 400$ m and $q_r = 0.48$ g m^{-3}, and using the turbulence levels ($\sigma_w = 0.4$ m s^{-1}, $\tau_w = 450$ s), we obtain the midcloud values for η shown in Fig. 17. The open triangles and circles give Electra-measured distributions for two 300-second (≈18 km) averages centered on the same symbols in Fig. 8, with $F_{\text{precip}} =$ 1.2 mm/day and 5.5 mm/day, respectively. The 260X measurements are known to underestimate the size concentrations in the 20–30-μm size classes (Baumgardner and Spowart 1990), and the sampling uncertainty at larger sizes, where concentrations fall below 10 m^{-3} is also apparent.

The autoconversion rates used in Fig. 17 for heavy and light precipitation ($A = 7 \times 10^{-9}$ kg m^{-3} s^{-1} and $A = 10^{-9}$ kg m^{-3} s^{-1}) are appropriate for adiabatic spectra in the upper half of the 14 July cloud. They correspond, for example, to $q_r = 0.48$ kg m^{-3} s^{-1}, $r_{\text{vol}} = 12.5$ μm, and $r_{\text{vol}} = 11.5$ μm (see Fig. 14), and demonstrate that (25) produces a close fit to midcloud precipitation spectra for a plausible choice of ($h, \tau_w, \sigma_w, q_r, A$). These autoconversion rates are not, however, values that we would infer from the FSSP measurements taken at midcloud in these precipitating regions. The subadiabatic liquid water content in the region of heavy drizzle is q_r = 0.2 g m^{-3}, and the autoconversion rate for the small droplet size distribution (circles in Fig. 17) is almost two orders of magnitude below that required to produce a 5.5 mm/day rain rate. Thus, although (25) captures the shape of the coalescence-produced drop size distribution, the steady-state assumption used to obtain (25) from the diffusing plume is unlikely to remain valid if scavenging depletes the small droplet population. We anticipate that this scavenging-induced decrease in the autoconversion rate may cause intermittent precipitation; we are investigating this possibility using nonequilibrium coalescence calculations with the numerical model described below.

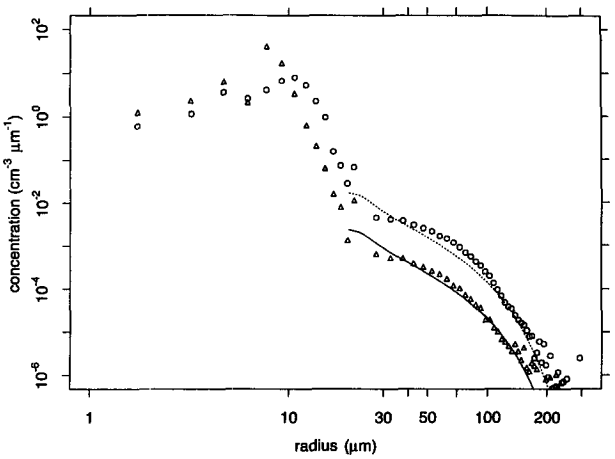

FIG. 17. Comparison of analytic model and Electra 260x observations. Boxes are 300-second (≈18 km) average beginning 18:43:26 UCT, 14 July leg L0 (see Fig. 8). Diamonds are 300-second average for 14 July leg L0 beginning 18:33:26 UCT. The two lines show the analytic model (25) with $A = 7 \times 10^{-9}$ kg m^{-3} s^{-1} (dotted) and $A = 10^{-9}$ kg m^{-3} s^{-1} (solid) and $h = 400$ m, $z = 200$ m, $\sigma_w = 0.4$ m s^{-1}, $\tau_w = 450$ s, $\tau_c = 23.3$ min.

2) TRANSILIENT MODEL

We can use the time-dependent transilient matrix model to test the existence of the steady-state assumed in the derivation of (25), while replacing the autoconversion and continuous collection parameterizations by an explicit solution to the stochastic collection equation. To proceed numerically, we partition the radius range into 60 logarithmically spaced bins with radii between 2 and 1800 μm. The smallest 20 of these bins, with radii between 2 and 18 μm, are specified by a distribution of the form of (12). No mass loss is permitted from these bins, but they contribute through both the autoconversion and accretion portions of the gain–loss integral (10) to the growth of the larger raindrop categories. At 20.1 μm and beyond, the concentrations in the remaining 40 categories are permitted to change under the influence of turbulence, coalescence, sedimentation, and condensation. Using $\vec{\eta}(z_i)$ to denote the vector of concentrations in the 60 size categories at height z_i, we have for the time rate of change of concentration

$$\frac{\partial \vec{\eta}}{\partial t} = \left(\frac{\partial \vec{\eta}}{\partial t}\right)_{\text{turb}} + \left(\frac{\partial \vec{\eta}}{\partial t}\right)_{\text{cond}} + \left(\frac{\partial \vec{\eta}}{\partial t}\right)_{\text{coal}} + \left(\frac{\partial \vec{\eta}}{\partial t}\right)_{\text{sed}}. \tag{26}$$

We solve (26) using split-time differencing: first calculating the gain or loss in bin k at time step $n-1$ by turbulent transport (with a 75-second time step), and then calculating the impact of condensation, coalescence, and sedimentation at each level of this new concentration profile (using a 2-second time step). The turbulence parameterization uses the transilient matrix c_{ij} to calculate the effect of mixing between times $n-1$ and n of all parcels bringing raindrops in size category k from level z_j to level z_i:

$$\eta_k^{(n)}(z_i) = [c_{ij}(\Delta t)][\eta_k^{(n-1)}(z_j)], \tag{27}$$

where the brackets indicate a matrix multiplication and Δt is the time step.

In appendix B we derive c_{ij}, given an autocorrelation function of the form (19), which allows us to directly compare the results of the analytic model (25) with our numerical model. As a test of (27), we can numerically model the plume of falling, accreting droplets shown in Fig. 16. We place a source of rate $A = 10^{-9}$ kg m^{-3} s^{-1} with $R_0 = 20$ μm at midlayer and construct the matrix c_{ij}, as in appendix B, with $\sigma_w = 0.4$ m s^{-1} and $\tau_w = 450$ s. The droplets are allowed to grow according to (21); the results of applying (27) to the initial profile shown in Fig. 16 are given by the open triangles (for $t = 12.5$ min) and open diamonds ($t = 50$ min) in the figure. The transilient matrix produces stronger initial diffusion than the analytic model (see Fig. B1) and overestimates the plume spreading rate at short times, but approaches the analytic result of (24) at later times.

The impact of coalescence is determined by solving (10) as described in section 4a, while the impact of precipitation is determined by first-order upstream differencing:

$$\left(\frac{\partial \vec{\eta}_k}{\partial t}\right)_{\text{sed}} = w_T^k \frac{\partial \vec{\eta}_k}{\partial z}, \tag{28}$$

where w_T^k, the terminal velocity for mass category k, is given by Beard (1976). Note that the terminal velocity varies only with droplet category, and so is constant in (28), and that vertical gradients of η_k are small. Replacing the upstream differencing with the more expensive hybrid scheme of Hall (1980) has no effect on the solution.

We include condensation by solving the droplet growth equation, neglecting curvature and solution effects and assuming that the supersaturation is at its equilibrium value for an updraft (or downdraft) of velocity W:

$$R\frac{dR}{dt} = \frac{S_{\text{eq}}}{F_k + F_d}. \tag{29}$$

Given values for the (assumed constant) coefficients F_k and F_d and the equilibrium supersaturation S_{eq}, we can write the contribution of condensation to the concentration change as

$$\left(\frac{\partial \eta(R,t,z)}{\partial t}\right)_{\text{cond}} = -\frac{\partial}{\partial R}\left[\frac{DR}{Dt}\eta(R,t,z)\right], \tag{30}$$

where we have used the continuous form of η for illustration.

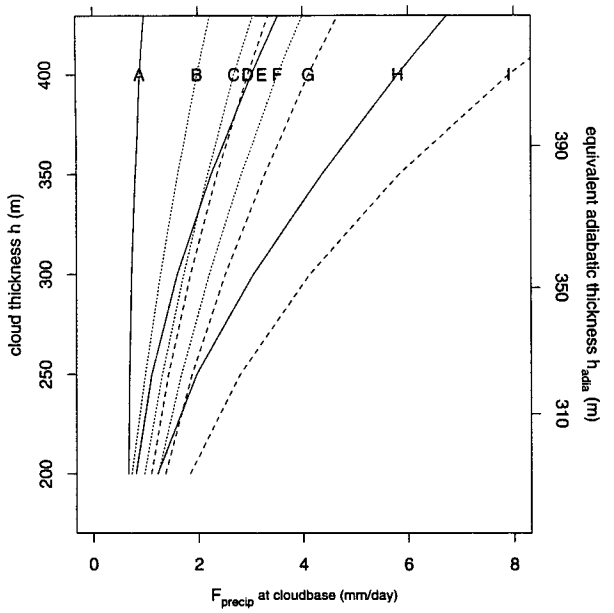

FIG. 18. Cloud-base precipitation flux F_{precip} (mm/day) vs cloud thickness for the analytic and numerical models, with cloud liquid water concentration $q_r = 0.48$ g m^{-3}. Solid lines show the numerical model with the Hocking and Jonas kernel, long dashed lines show the numerical model with a constant collection efficiency, and short dashed lines show the analytic solution. (A) Numerical model, Hocking and Jonas kernel, $r_{vol} = 10.5$ (no condensation). (B) Analytic solution, $E_c = 0.5$. (C) Analytic solution, $E_c = 0.6$. (D) Numerical model, $E_c = 0.5$. (E) Numerical model, Hocking and Jonas kernel, $r_{vol} = 10.5$ μm, with condensation. (F) Analytic solution, $E_c = 0.7$. (G) Numerical model, $E_c = 0.6$. (H) Numerical model, Hocking and Jonas kernel, $r_{vol} = 11$ μm, with condensation. (I) Numerical model, $E_c = 0.7$. The right axis gives h_{adia}, the equivalent thickness of an adiabatic cloud (see text).

We solve (30) using the semi-Lagrangian advection scheme of Bott et al. (1990). We infer S_{eq} for these clouds by (e.g., Cooper 1989)

$$S_{eq} = \frac{cW}{N_r\langle r\rangle}, \tag{31}$$

where N_r and $\langle r\rangle$ are the number concentration and mean radius for the constant small droplet population in bins 1–20.

The vertical velocity W due to turbulent transport during the time step is inferred from the heights of z_i and z_j and the time step Δt ($W = (z_i - z_j)/\Delta t$). It is set to a maximum value of $|W| = 0.5$ m s^{-1} for $|W| > 0.5$ m s^{-1}, which spans 95% of the velocities observed in these layers. Because all transitions are represented in the transilient matrix, placing this kind of a constraint on W reduces the condensation growth experienced by parcels making large vertical transitions (from, for instance, layer bottom to layer top).

We will consider the coefficients in (29) and (31) to be constant throughout these shallow stratocumulus layers. For temperatures of ≈280 K and pressures of ≈950 hPa, we have $1/(F_k + F_d) \approx 1 \times 10^{-10}$ m^2 s^{-1}, $c \approx 1.6$ m^{-3} s. This implies that for a typical precipitating cloud, with $N \approx 100$ cm^{-3} and $r_{vol} \approx 10.5$ μm, the equilibrium supersaturation S_{eq} used in (31) will not exceed ±0.15%, and will usually be significantly less. In mixed parcels with lower droplet concentrations the super- (and sub-) saturation could frequently be 2–3 times greater than this value. We consider (29) to be a lower bound on the impact of condensation (and evaporation) on raindrop production.

5. Sensitivity to cloud thickness and the coalescence kernel

In Fig. 18 we compare the sensitivities of the precipitation flux at cloud base predicted by the analytic and numerical models to cloud thickness, the collection efficiency, and the small droplet distribution, and in Fig. 19 we show the corresponding raindrop size distributions at midcloud in a 400-m-thick cloud. There are three groups of three lines: the dotted lines B–C–F (analytic) show the integrated precipitation flux using (25) with collection efficiencies in (21) of $E_c = (0.5, 0.6, 0.7)$, using cloud water content $q_r = 0.48$ g m^{-3} and an autoconversion rate of $A = 3.8 \times 10^{-9}$ kg m^{-3} s^{-1}. Although the numerical model can calculate the evolution of precipitation given an arbitrary liquid water profile, we assume q_r constant with height in this example to permit a direct comparison with the analytic solution. The right axis uses (6) to show the thickness h_{adia} needed by an adiabatic cloud to produce the same liquid water path as a cloud of depth h and constant $q_r = 0.48$ g m^{-3}: $1.15 \times 10^{-3} h_{adia}^2 = 0.48h$ (g m^{-3}). The dashed lines D–G–I give the numerical results for the same constant collection efficiencies and droplet size distribution (constant with height) Γ_2 with

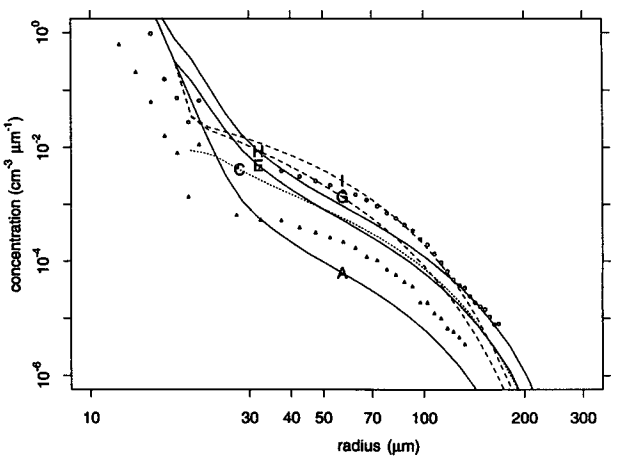

FIG. 19. Precipitation spectra at $z = 200$ m in a 400-m thick cloud for the conditions of Fig. 18. Line labels are the same as in Fig. 18, the circles and triangles show the 60-second average precipitation spectra of Fig. 17.

$\nu = 0.3$. The autoconversion rate from (15) for this distribution is $\approx 9.5 \times 10^{-10}$ kg m^{-3} s^{-1}.

The curve pairs D–B, G–C, and I–F present the difference between the stochastic collection calculation and continuous collection, given equal collection efficiencies. As expected, the stochastic collection scheme produces higher rain rates than continuous collection at all cloud thicknesses, with the difference increasing rapidly with cloud depth and collection efficiency. This greater precipitation production occurs despite the fact that the autoconversion rate used in the numerical model is ≈ 3.5 times lower than that used in the analytic solution (9.5×10^{-10} vs 3.8×10^{-9} kg m^{-3} s^{-1}). The midcloud raindrop spectra for curves G and C are included in Fig. 19. The analytic solution, which has a lower rain rate than the numerical solution at midcloud, actually has higher concentrations of raindrops with $R > 100$ μm for the same collection efficiency. This is due to the analytic solution's cloud top "reentry" of large drops mentioned in the discussion of Fig. 16.

The average collection efficiency for the hydrodynamic kernel, weighted by a fully developed precipitation spectrum, is approximately $\overline{E_c} = 0.5$. We might expect that replacing the constant kernel $E_c = 0.5$ (curve D) in Fig. 18 by the hydrodynamic kernel in the numeric model would produce similar precipitation fluxes. Instead the precipitation rate at the base of a 400-m-thick cloud falls to 0.9 mm/day (curve A). This is due to the low collection efficiencies for raindrops with radii < 23 μm ($\overline{E_c} < 0.05$). Increasing the autoconversion rate has little impact on the precipitation flux (not shown) because the additional small raindrops sediment out of the cloud before they can coalesce. When the effects of condensation are included (solid curve E), the equilibrium precipitation increases to 3 mm/day, as 20 μm raindrops are able to grow to sizes with larger collection efficiencies. Comparing curves E and G in Fig. 19 shows that the additional raindrop supply provided by condensation increases the number of raindrops with $R > 100$ μm to a level equivalent to the analytic solution with $E_c = 0.6$ (curve C).

The numerical model is also significantly more sensitive to changes in autoconversion when condensation is included. The solid curves labeled H in Figs. 18 and 19 show the impact of replacing the Γ_2 distribution with Γ_3 ($r_{vol} = 11.5$ μm, $N_r = 75$ cm^{-3}, $q_r = 0.48$ g m^{-3}, $\nu = 0.3$). The new autoconversion rate is $A = 4.3 \times 10^{-9}$ kg m^{-3} s^{-1} (4.5 times larger), and the precipitation flux increases from 3 to 5.8 mm/day for a 400-m-thick cloud. Without condensation, the precipitation flux drops to 1.44 mm/day. Comparing the spectra for curves E ($r_{vol} = 10.5$ μm) and H ($r_{vol} = 11.5$ μm) shows that the larger supply of small droplets results in a constant relative increase in the raindrop concentration at all sizes.

The role of condensation growth in helping to initiate coalescence in cumulus updrafts is well known (Leighton and Rogers 1974; Jonas and Mason 1974). Nicholls (1987), however, found little sensitivity to condensation (and no need to invoke condensation to produce drizzle drops) in his precipitation model. As we mentioned in section 4a, we have used the Jonas and Mason (1974) kernel used by Nicholls in sensitivity tests. Our results differ from his in that we find that significant coalescence cannot occur without assistance from condensation growth.

6. Discussion

We have presented aircraft and satellite observations of stratocumulus clouds that show relatively complex spatial and temporal variations in precipitation and cloud optical depth. On the one hand, the cloud layers are characterized by large horizontal variations in cloud-base and cloud-top heights, and by localized regions of precipitation large enough to cause cloud water depletion. However, these precipitation events do not seem to determine the regional distribution of cloud thickness or cloud fraction, which remains high over the course of each day. The satellite retrievals for 30 June, for example, show a decrease in median optical depth of less then five between sunrise and sunset, although aircraft observations indicated large precipitation rates at midcloud during this day. During the period from local noon to 1700, the optical depth changes by less than 2. On 14 July, in thicker cloud, the regional median optical depth remains between 16 and 20 throughout most of the afternoon, and by sunset still exceeds 13, implying a cloud thickness in excess of 250 m.

The observations also show that clouds with markedly different liquid water paths and droplet size distributions can have similar precipitation rates. Comparison of the microphysical measurements along level legs and in vertical soundings for 30 June and 14 July show that the two clouds differ by more than a factor of 2 in droplet number concentration and by 60% in cloud liquid water path, but produce roughly equal precipitation fluxes. They have in common the fact that r_{vol} exceeds 10 μm through most of both layers. A counterexample is 16 July, but low aircraft-measured liquid water content suggest that the aircraft may have been below the region of active precipitation in the 16 July cloud.

Calculated autoconversion rates provide evidence that precipitation in stratocumulus clouds should be sensitive to the size of the cloud droplets. The 30 June layer produces rain with cloud droplets ranging from 10 to 13 μm and coalescence with these targets occurs in a region of the hydrodynamic kernel in which the collision efficiency varies rapidly with droplet size. Changes of 10% in the mean radius or distribution relative variance, if they occur throughout the cloud, can increase the creation rate of embryonic raindrops by an order of magnitude. Both the analytic and numerical calculations presented here suggest that, given collec-

tion efficiencies that permit growth of these 20-μm drops to 30 μm or larger, the precipitation flux will be sensitive to variations in the autoconversion rate typical of a 1–2 μm change in cloud droplet volume mean radius.

Our numerical results indicate that, over a period of 1–2 hours, a steady-state balance between coalescence, turbulence, and sedimentation can be established, provided that enough new droplets are produced to maintain a constant autoconversion rate. The raindrop distributions generated by the numerical model, including condensation growth and coalescence with a hydrodynamic kernel, are similar to analytic equilibrium distributions for a continuously collecting, diffusing plume of drizzle drops. We have explored a very limited range of parameter values for these models, varying only the collection kernel, the autoconversion rate, and cloud thickness, with a fixed Gaussian distribution of vertical velocities. Within this range of parameters, the equilibrium droplet spectra of the analytic and numerical models resemble observations of raindrop-size distributions observed at midcloud. The success of the analytic model in matching these distributions, given its simple autoconversion and collection parameterizations, suggests that a one-dimensional equilibrium calculation may capture an important part of the physics of stratocumulus rainfall.

In this initial study we have excluded a number of effects that could influence precipitation initiation. For example, giant CCN could play an important role in triggering coalescence in these layer clouds (Beard and Ochs 1993), although the turbulence-extended droplet lifetimes appear to be long enough to produce coalescence without extremely large aerosols. We are currently modifying the one-dimensional numerical model to include a vertically varying droplet size distribution, the impact of radiation on droplet growth, and a time-dependent response to precipitation scavenging.

Additional ground-based, satellite, and aircraft observations of both equilibrium and time-dependent precipitation are needed to more tightly link the cloud microphysical character to the rain rate, to determine the impact of precipitation on regional cloud radiative properties, and to constrain the precipitation parameterizations needed for large-scale models. Some of these measurements have already been made: the Atlantic Stratocumulus Transition Experiment (ASTEX) has provided a dataset that should help address many of the questions raised by this analysis of FIRE precipitation.

Acknowledgments. We gratefully acknowledge helpful discussions with Marcia Baker on her stochastic precipitation model and the valuable comments of three anonymous reviewers. Jiujing Gu and Goska Szczodrak provided valuable assistance with the radiative transfer modeling and satellite image processing. We would also like to thank the NCAR Research Aviation Facility for providing and processing the Electra aircraft data, Darrel Baumgardner for his microphysical probe-correction subroutines, and Doug Johnson and Gill Martin of the British Meteorological Office, and Keith Bower of the University of Manchester Institute of Science and Technology for the C130 data. Yefim Kogan kindly provided his implementation of the Berry and Reinhardt stochastic collection algorithm. We thank NASA Goddard's NSSDC for the GOES imagery, and the NASA Goddard Climate and Radiation Branch for AVHRR imagery and navigation software. Our work has benefited from public domain software provided by the National Center for Supercomputer Applications (HDF), the University of Hawaii (GMT), and Scott Katz of the University of Washington (Satview). RP gratefully acknowledges support from a NASA Graduate Fellowship in Global Change Research NGT-30047. This work was supported by the National Science and Engineering Research Council of Canada and the Atmospheric Environment Service.

APPENDIX A

Instrumentation

a. Particle counting and sizing errors

We use droplet and raindrop concentration measurements as a function of radius $n(r)$ (m^{-3} μ^{-1}) made by two PMS microphysical probes operating at 10 Hz: an FSSP set on these flights to size particles with radii between 1 μm $< r <$ 23.5 μm in 1.5-μm wide bins and a PMS 260X, which spans a radius range of 20 μm $< R <$ 310 μm in 5-μm wide bins (with the two missing bins noted below). The inhomogeneous beam and sample volume corrections of Baumgardner and Spowart (1990) were applied to the FSSP measurements, and bin-dependent sample volume corrections (D. Baumgardner 1990, personal communication) were applied to the 260X measurements.

1) FSSP MEASUREMENTS OF LARGE LIQUID WATER CONTENTS

The JLWC and FSSP liquid water content soundings presented in Fig. 6 differ much of the time by more than 50% and show subadiabatic liquid water contents for most soundings. Recently, Gerber et al. (1993) did an in-cloud comparison (1992 ASTEX Experiment, University of Washington C-131 aircraft) of an FSSP and a new optical sensor (the PVM-100A), which measures integrated cloud liquid water by forward light scattering. In a 345-m thick cloud that exhibited little evidence of entrainment and no precipitation the PVM probe measured liquid water contents >90% of adiabatic throughout the cloud, while the FSSP measured adiabatic liquid water contents in the lower half of the cloud and liquid water contents in the upper half of the cloud that were ≈60% of adiabatic. The FSSP liquid

water measurements presented here have been brought closer to adiabatic values using the time response and laser inhomogeneity corrections of Baumgardner and Spowart (1990). These corrections increase FSSP-measured liquid water contents by 20%–30% in most cases. The corrected Electra FSSP consistently measures higher water contents than the Electra Johnson–Williams probe, the reverse of situation for the two C130 instruments. More comparisons are clearly needed, and all FSSP measurements presented of the upper portions of these thick, precipitating clouds should be regarded as tentative.

The Electra FSSP bin 15 ($22 < r < 23.5$ μm) and the 260X bin 1 ($20 < r < 25$ μm) are both missing for these FIRE flights. If we fill the gap between 22–25 μm with interpolated values for the spectra in Fig. 17, the FSSP volume mean radius is increased by <0.3% and the precipitation flux is increased by <0.1%.

2) 260X COUNTING AND SIZING UNCERTAINTIES

In Fig. A1 we show two 60-second samples through regions of the 14 July cloud with low [Fig. A1(a)] and high [Fig. A1(b)] precipitation rates. The solid lines show the raw counts, uncorrected for the sample volume, from the FSSP and 260X probes as a function of bin radius. The dashed lines show, following (Nicholls 1984) three estimates of the cumulative precipitation flux $f_{\text{precip}}(R)$ defined by

$$f_{\text{precip}}(R_n) = 4/3\pi\rho_w \sum_{i=1}^{n} w_T(R_i) R_i n(i) \Delta R. \quad \text{(A1)}$$

The middle line indicates the actual estimate, while the upper and lower lines show the effect of consistently oversizing or undersizing the precipitation particles by a single bin. At typical stratocumulus precipitation rates of 1.4 mm/day [Fig. A1(a)] there are 1818 raindrops sampled by the 260X. The FSSP-measured droplets contribute a background precipitation flux (neglecting turbulence) of ≈0.3 mm/day. The definition of F_{precip} in (7) neglects this contribution, and the precipitation fluxes will be calculated using only the 260X values.

At higher rain rates, Fig. A1(b) shows that the distribution shape is relatively unchanged with the mean radius for drizzle drops increasing from $R = 46$ μm to $R = 48$ μm. The number of raw counts and the concentration has increased by a factor of 8, with counts in the 50 μm $< R <$ 150 μm range between 10 and 650. Under- or oversizing introduces flux errors of roughly 20%–30% at these larger precipitation levels.

We will use 60-second horizontal averages when the drizzle concentration is consistently smaller than 0.05 cm^{-3} to insure that there are at least 10 counts in each of the 50 μm $< R <$ 150 μm channels. We will increase our horizontal resolution by using 20-second averages at higher concentrations, when the shorter averaging time does not change the calculated mean rain rate.

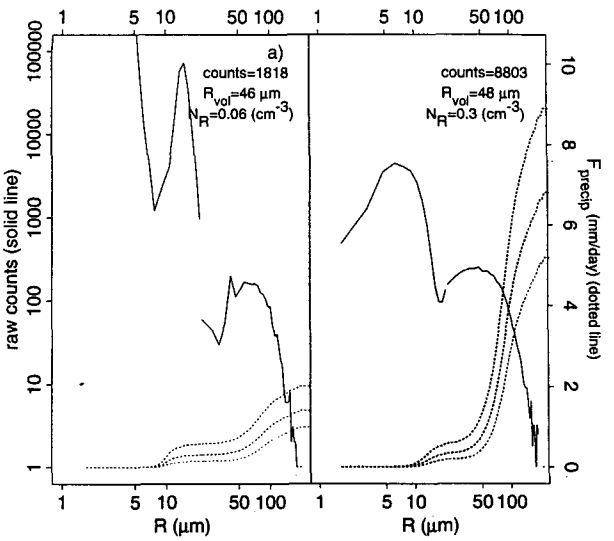

FIG. A1. Solid line shows probe counts without sample volume correction for the FSSP and 260X for a 60-second sample time during light (a) and heavy (b) precipitation in the 14 July cloud. Dotted line shows cumulative precipitation flux $f_{\text{precip}}(R)$.

b. *Vapor flux measurements*

We measured vapor fluxes with the fast-response (20 Hz) Lyman-α hygrometer, calibrated against a dew-point hygrometer for each flight leg and the differential pressure vertical velocity probe for 20 Hz velocity measurements. The velocity measurement undergoes spurious fluctuations (Paluch and Lenschow 1991), particularly during transitions between precipitation and clear air. These segments were deleted from the mean flux calculation. There is also evidence (Paluch and Lenschow 1991) that the vertical velocity measurement may be overestimating the vapor flux by 10%–30%.

APPENDIX B

Computation of the transilient coefficients C_{ij}

We follow Stull (1984) and assume that the coefficients c_{ij} of the transilient matrix of (27) will scale as W/D^2, where W and D are the velocity and distance scales for interchange between the heights z_i and z_j. We set D equal to ζ, the distance between the destination layer at height z_i and the source layer z_j. The wavenumber associated with ζ is $k = 2\pi/\zeta$, and the velocity variance between ln$k$ and ln$k$ + Δ ln$k$ is approximately given by

$$W^2 = \int_{\Delta \ln k} kE(k) d \ln k \approx kE(k), \quad \text{(B1)}$$

where $E(k)$ is the power spectral density and we have chosen $\Delta \ln k = 1$ (Tennekes and Lumley 1972).

To compute $E(k)$ we use the autocorrelation given by (19) and assume that the Lagrangian and Eulerian timescales are roughly equal (see, e.g., Hunt 1981). With this assumption, (19) becomes

$$R(r) = \sigma_w^2 \exp(-|r|/r_E)$$

$$E(k) = \frac{2}{\pi}\int_0^\infty R(r)\cos(kr)dr = \frac{2}{\pi}\left(\frac{\sigma_w^3\tau_w}{1+\sigma_w^2\tau_w^2k^2}\right)$$

$$W/D^2 \approx (kE(k))^{(1/2)}/\zeta^2 = c(\Delta t)_{ij} = \frac{1}{\zeta^2}\left(\frac{4\sigma_w^3\tau_w\zeta}{\zeta^2+4\pi^2\sigma_w^2\tau_w^2}\right)^{(1/2)}, \quad \text{(B2)}$$

where r is the Eulerian distance and $r_E \approx \sigma_w\tau_w$ is an Eulerian length scale.

The expression for $c(\Delta t)_{ij}$ in (2) gives the fraction mixed to layer i from a layer a distance ζ away (i.e., it provides terms for one horizontal row of the transilient array). If the turbulence is homogeneous, all rows are identical and the matrix can be assembled by stacking rows to a depth matching the model domain, with each row offset so that the point $\zeta = 0$ lies on the diagonal.

To complete the transilient matrix we need to apply boundary conditions and choose a time step Δt and a cutoff scale ζ_c, which limits the size of the eddies that do the mixing (Stull 1984). We typically choose a domain of 100 levels with $\Delta z = 10$ m and $\zeta_c = 100$ m, and enforce conservation as Stull suggests, "folding" those values of the matrix that lie outside the domain onto the diagonal for each row. This essentially prohibits mixing above cloud top or below the bottom layer.

To set the time step we use Stull's Eq. (20):

$$[c(n\delta t)] = [c(\delta t)]^n. \quad \text{(B3)}$$

Stull suggests that δt scales with the viscous-subscale time range, roughly 0.06 s for these clouds. Our approach is to specify $n\delta t = 75$ s, and then choose n in (B3) so that the evolution of the standard deviation (σ_{zt}) of concentration for a spreading plume calculated using (27) matches the result from Taylor's theorem:

$$\sigma_{zt} = \tau_w\sigma_w[2(t/\tau_w - 1 + \exp(-t/\tau_w))]^{1/2}. \quad \text{(B4)}$$

Figure B1 shows two such calculations. The triangles show plume spreading with $\sigma_w = 0.4$ m s^{-1}, $\tau_w = 20$ s, and $n = 64$, while the squares show $\sigma_w = 0.4$ m s^{-1}, $\tau_w = 300$ s, and $n = 2304$. The lines in each case show σ_z computed from (B4). At larger τ_w, the plume growth is more rapid than predicted by (B4), but there exists a choice of n, increasing with increasing τ_w, for each of the examples used in this paper that produces an asymptotic approach to the spreading rate predicted by Taylor's theorem.

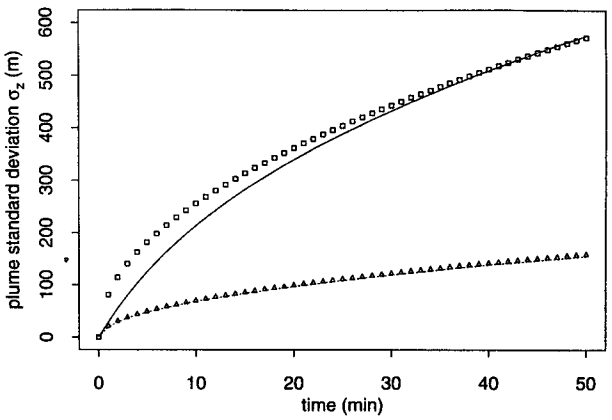

FIG. B1. Comparison of plume growth for analytic and transilient models. Dotted line shows (B4) with $\sigma_w = 0.4$ m s^{-1} and $\tau_w = 20$ s. Triangles show plume evolution from (27) with c_{ij} constructed using (B3) with identical τ_w, σ_w, $n = 64$. Solid line shows (B4) with $\sigma_w = 0.4$ m s^{-1} and $\tau_w = 300$ s. Squares show (27) with this σ_w, τ_w, $n = 2304$.

REFERENCES

Albrecht, B., 1989: Aerosols, cloud microphysics and fractional cloudiness. *Science,* **245,** 1227–1230.

——, D. A. Randall, and S. Nicholls, 1988: Observations of marine stratocumulus during FIRE. *Bull. Amer. Meteor. Soc.,* **69,** 618–626.

Baker, M. B., 1993: Variability in concentrations of cloud condensation nuclei in the marine cloudtopped boundary layer. *Tellus,* **45B,** 458–472.

——, and R. J. Charlson, 1989: Bistability of CCN concentrations and thermodynamics in the cloud-topped boundary layer. *Nature,* **345,** 142–144.

Baumgardner, D., and M. Spowart, 1990: Evaluation of the Forward Scattering Spectrometer Probe. Part III: Time response and laser inhomogeneity limitations. *J. Atmos. Oceanic Technol.,* **7,** 666–672.

Beard, K. V., 1976: Terminal velocity and shape of cloud and precipitation drops aloft. *J. Atmos. Sci.,* **33,** 851–864.

——, and H. T. Ochs, 1993: Warm-rain initiation: An overview of microphysical mechanisms. *J. Appl. Meteor.,* **32,** 608–625.

Berry, E. X., and R. L. Reinhardt, 1973: Modeling of condensation and collection within clouds. Physical Science Publication No. 16, Desert Research Institute, University of Nevada at Reno, 96 pp.

——, and ——, 1974a: An analysis of cloud drop growth by collection: Part I. Double distributions. *J. Atmos. Sci.,* **31,** 1814–1824.

——, and ——, 1974b: An analysis of cloud drop growth by collection: Part II. Single initial distributions. *J. Atmos. Sci.,* **31,** 1825–1831.

Betts, A. K., 1990: Diurnal variation of California coastal stratocumulus from two days of boundary layer soundings. *Tellus,* **42A,** 302–304.

Boers, R., and A. Betts, 1988: Saturation point structure of marine stratocumulus clouds. *J. Atmos. Sci.,* **45,** 1156–1175.

Bott, A., U. Sievers, and W. Zdunkowski, 1990: A radiation fog model with a detailed treatment of the interaction between radiative transfer and fog microphysics. *J. Atmos. Sci.,* **47,** 2153–2166.

Brost, R. A., D. H. Lenschow, and J. C. Wyngaard, 1982a: Marine stratocumulus layers. Part II: Turbulence budgets. *J. Atmos. Sci.,* **39,** 818–836.

——, ——, and ——, 1982b: Marine stratocumulus layers. Part I: Mean conditions. *J. Atmos. Sci.,* **39,** 800–817.

Chen, C., and W. R. Cotton, 1987: The physics of the marine stratocumulus-capped mixed layer. *J. Atmos. Sci.*, **44,** 2951–2977.

Cooper, W. A., 1989: Effects of variable droplet growth histories on droplet size distributions. Part I: Theory. *J. Atmos. Sci.*, **46,** 1301–1311.

Davis, M. H., and J. D. Sartor, 1967: Theoretical collision efficiencies for small cloud droplets in stokes flow. *Nature,* **215,** 1371–1372.

de Almedia, F. C., 1977: Collision efficiency, collision angle and impact velocity of hydrodynamically interacting cloud drops: A numerical study. *J. Atmos. Sci.*, **34,** 1286–1292.

Desormeaux, Y., W. B. Rossow, C. L. Brest, and G. Campbell, 1993: Normalization and calibration of geostationary satellite radiances for the International Satellite Cloud Climatology Project. *J. Atmos. Oceanic Technol.*, **10,** 304–325.

Gerber, H., B. G. Arends, and A. S. Ackerman, 1994: New microphysics sensor for aircraft use. *Atmos. Res.*, **31,** 235–251.

Hall, W. D., 1980: A detailed microphysical model within a two-dimensional dynamic framework: Model description and preliminary results. *J. Atmos. Sci.*, **37,** 2486–2507.

Hocking, L. M., and P. R. Jonas, 1970: The collision efficiency of small drops. *Quart. J. Roy. Meteor. Soc.*, **96,** 722–729.

Hudson, J. G., and P. R. Frisbie, 1991: Cloud condensation nuclei near marine stratus. *J. Geophys. Res.*, **96,** 20 795–20 808.

Hunt, J. C. R., 1981: Diffusion in the SBL. *Atmospheric Turbulence and Air Pollution Modelling: A Course Held in The Hague,* 21–25 September 1981, F. Nieuwstadt and H. van Dop, Eds, D. Reidel, 231–274.

Johnson, D., 1982: The role of giant and ultragiant aerosol particles in warm rain initiation. *J. Atmos. Sci.*, **39,** 448–460.

Jonas, P., and B. J. Mason, 1974: The evolution of droplet spectra by condensation and coalescence in cumulus clouds. *Quart. J. Roy. Meteor. Soc.*, **100,** 286–295.

Kloesel, K. A., B. A. Albrecht, and D. P. Wylie, 1988: FIRE marine stratocumulus observations-summary of operations and synoptic conditions. FIRE Tech. Rep. No. 1, The Pennsylvania State University, Dept. of Meteorology, University Park, PA, 171 pp.

Leighton, H. G., and R. R. Rogers, 1974: Droplet growth by condensation and coalescence in a strong updraft. *J. Atmos. Sci.*, **31,** 271–279.

Liou, K. N., and S. C. Ou, 1989: The role of cloud microphysical processes in climate: An assessment from a one-dimensional perspective. *J. Geophys. Res.*, **94,** 8599–8607.

Minnis, P., P. W. Heck, D. F. Young, C. W. Fairall, and J. B. Snider, 1992: Stratocumulus cloud properties derived from simultaneous satellite and island-based instrumentation during FIRE. *J. Appl. Meteor.*, **31,** 317–339.

Nakajima, T., M. D. King, J. D. Spinhirne, and L. F. Radke, 1991: Determination of the optical thickness and effective particle radius of clouds from reflected solar radiation measurements. Part II: Marine stratocumulus observations. *J. Atmos. Sci.*, **48,** 728–750.

Nicholls, S., 1984: The dynamics of stratocumulus: Aircraft observations and comparisons with mixed layer models. *Quart. J. Roy. Meteor. Soc.*, **110,** 783–820.

——, 1987: A model of drizzle growth in warm, turbulent, stratiform clouds. *Quart. J. Roy. Meteor. Soc.*, **113,** 1141–1170.

——, and J. Leighton, 1986: An observational study of the structure of stratiform cloud sheets: Part I. Structure. *Quart. J. Roy. Meteor. Soc.*, **112,** 431–460.

Paluch, I. R., and D. H. Lenschow, 1991: Stratiform cloud formation in the marine boundary layer. *J. Atmos. Sci.*, **48,** 2141–2158.

Pasquil, F., and F. B. Smith, 1983: *Atmospheric Diffusion.* Elis Horwood Ltd, 437 pp.

Pincus, R., M. Baker, and C. Bretherton, 1992: Lagrangian observations of marine stratocumulus evolution and breakup. *Proc. 11th Int. Conf. on Clouds and Precipitation,* Montreal, Canada, ICCP/IAMAP, 362–365.

Reinhardt, R. L., 1972: An analysis of improved numerical solutions to the stochastic collection equation for cloud droplets. Ph.D. Thesis, University of Nevada, Reno, 111 pp.

Richard, E., and N. Chaumerliac, 1989: Effects of different rain parameterizations on the simulation of mesoscale orographic precipitation. *J. Appl. Meteor.*, **28,** 1197–1211.

Rossow, W. B., L. C. Garder, and A. A. Lacis, 1989: Global, seasonal cloud variations from satellite radiance measurements. I. Sensitivity of analysis. *J. Climate,* **2,** 419–458.

Scott, W. T., 1968: Analytic studies of cloud droplet coalescence I. *J. Atmos. Sci.*, **25,** 54–65.

Stull, R. B., 1984: Transilient turbulence theory. Part I: The concept of eddy-mixing across finite distances. *J. Atmos. Sci.*, **41,** 3351–3367.

Tennekes, H., and J. L. Lumley, 1972: *A First Course in Turbulence.* MIT Press. 300 pp.